

Vacuum technology for particle accelerators

Paolo Chiggiato

CERN, 1211 Geneva 23, Switzerland

Abstract

This note covers part of the JUAS lecture about ‘vacuum technology for particle accelerators’. Some subjects are not yet integrated, for example the description of instrumentation and vacuum control; they will be added in the next years. The description is far to be exhaustive; however, it gives the basis to understand, assess, and appreciate the work of vacuum specialists.

1 Introduction

The knowhow of vacuum technology is a multidisciplinary. Knowledge of material science and mechanical engineering are indispensable in the phase of design and production. Surface treatments and coatings are crucial to achieve the required beam pipes characteristics. Surface science and simulation are essential to anticipate the behaviour of a vacuum system and understand its interaction with the beams. Instrumentation and control software provide monitoring, protection, interlocks and signals for other equipment.

The goal of vacuum systems is to remove the gas load generated by thermal outgassing, beam induced desorption, and intentional gas injection to achieve the required beam lifetime. In addition, vacuum protects high-voltage equipment and provides the thermal insulation for cryogenic systems.

Pressure requirements, the gas load, and long duty time impose a drastic selection of the vacuum pumps and the way they are operated. Mechanical pumps are the obvious choice close to the injection points, where the gas throughput is the highest (for example gas sources). Such pumps evacuate the gas molecules outside the vessel. However, as soon as most of the injected gas is evacuated and lower pressures must be reached, the vacuum system should rely on capture pumps because they are in general more reliable than mechanical pumps.

The evaluation of pressure profiles with and without circulating beams should be undertaken in parallel with the mechanical design. Basic calculations may be carried out for simple geometries. However, the complexity of the mechanical design requires advanced computation. The molecular trajectories in the vacuum system are simulated by Monte Carlo codes and pressures are evaluated by counting the molecular collisions with virtual surfaces. The analogy between vacuum systems and electrical networks, in conjunction with the Monte Carlo simulations, may be used to obtain time-dependent pressure profiles.

In accelerators, pressure is measured applying different principles. In the highest pressures range, nearby ion sources, mechanical and thermal conductivity effects are still significant in the gas phase. In this case, thermal and capacitance pressure gauges are employed. For a more rarefied gas, pressure readings are obtained by measuring gas-ion currents intentionally produced by electron impact ionisation.

2 Basic notions of vacuum technology

In the framework of vacuum technology for particle accelerators, a rarefied gas in equilibrium is always described by the ideal-gas equation of state:

$$P V = N_{moles} R T \quad (1)$$

where P, T and V are the gas pressure, temperature and volume, respectively; R the ideal gas constant (8.314 J K⁻¹ mol⁻¹ in SI units) . From statistical physics considerations, Eq. 1 may be rewritten in terms of the total number of molecules N in the gas:

$$P V = N k_B T \quad (2)$$

k_B is the Boltzmann constant (1.38 10⁻²³ J K⁻¹ in SI units).

In the International System of Units, the pressure is reported in Pa: 1 Pa is equivalent to the pressure exerted by one N on a m². Other units are regularly used in vacuum technology, in particular bar and its submultiple the mbar. The Torr is still occasionally used, mostly in the USA; it is equivalent to the pressure exerted by a one-mm high column of Hg. The conversion values between the common pressure units are collected in Tab.1.

Table 1: conversion values for the most common pressure units of vacuum technology

| | Pa | Bar | atm | Torr |
|--------|-----------------------|-----------------------|------------------------|----------------------|
| 1 Pa | 1 | 10 ⁻⁵ | 9.87 10 ⁻⁶ | 7.5 10 ⁻³ |
| 1 bar | 10 ⁵ | 1 | 0.987 | 750.06 |
| 1 mbar | 10 ² | 10 ⁻³ | 0.967 10 ⁻³ | 0.75 |
| 1 atm | 1.013 10 ⁵ | 1.013 | 1 | 760 |
| 1 Torr | 133.32 | 1.33 10 ⁻³ | 1.32 10 ⁻³ | 1 |

The number density ($n = N/V$) of gas molecules is easily calculated by Eq. 2. Some typical examples are collected in Tab. 2.

Table 2: Typical number density at room temperature and helium boiling point

| | Pressure | 293 K | 4.3K |
|---|-----------------------|------------------------------------|------------------------------------|
| | [Pa] | [molecules cm⁻³] | [molecules cm⁻³] |
| Atmospheric pressure at sea level | 1.013 10 ⁵ | 2.5 10 ¹⁹ | 1.7 10 ²¹ |
| Typical plasma chambers | 1 | 2.5 10 ¹⁴ | 1.7 10 ¹⁶ |
| Linac pressure upper limit | 10 ⁻⁵ | 2.5 10 ⁹ | 1.7 10 ¹¹ |
| Lowest pressure ever measured at room temperature [1] | 10 ⁻¹² | 250 | 1.7 10 ⁴ |

In addition to the number of molecules or moles, gas quantities are expressed as pressure-volume (PV) values at a given temperature. Pressure-volume quantities are converted to number of molecules dividing them by $k_B T$ as given in the equation of state. For example, 1 Pa m³ at 293 K is equivalent to:

$$N = \frac{1 [\text{Pa} \cdot \text{m}^3]}{1.38 \cdot 10^{-23} \left[\frac{\text{J}}{\text{K}} \right] 293 [\text{K}]} = 2.47 \cdot 10^{20} \text{ molecules}$$

In the same way, at 293 K, 1 Torr $\ell = 3.3 \cdot 10^{19}$ molecules and 1 mbar $\ell = 2.47 \cdot 10^{19}$ molecules. In vacuum technology, pressure-volume units are used most of the time to report gas quantities and flow rates. For example, the gas flow rate is generally reported in mbar $\ell \text{ s}^{-1}$ or Torr $\ell \text{ s}^{-1}$.

In vacuum systems, pressures span several orders of magnitude. Degrees of vacuum are defined by upper and lower pressure boundaries. Different degrees of vacuum are characterised by different pumping technologies, pressure measurement, materials, and surface treatments. For example, ion sources operate in the degrees of vacuum that are usually called medium and high vacuum, while in the LHC experimental beam pipes the extreme vacuum range is attained.

Table 3: Degrees of vacuum and their pressure boundaries

| | Pressure boundaries [mbar] | Pressure boundaries [Pa] |
|-----------------------|-------------------------------------|-------------------------------------|
| Low Vacuum LV | 1000-1 | 10 ⁵ -10 ² |
| Medium Vacuum MV | 1-10 ⁻³ | 10 ² -10 ⁻¹ |
| High Vacuum HV | 10 ⁻³ -10 ⁻⁹ | 10 ⁻¹ -10 ⁻⁷ |
| Ultra High vacuum UHV | 10 ⁻⁹ -10 ⁻¹² | 10 ⁻⁷ -10 ⁻¹⁰ |
| Extreme Vacuum XHV | <10 ⁻¹² | <10 ⁻¹⁰ |

2.1 Gas kinetics

The kinetics of ideal-gas molecules is described by the Maxwell-Boltzmann theory [2]. For an isotropic gas, the model provides the probabilistic distribution of the molecular speed magnitudes. The mean speed of molecules $\langle v \rangle$, i.e. the mathematical average of the speed distribution, is given by Eq.3.

$$\langle v \rangle = \sqrt{\frac{8 k_B T}{\pi m}} = \sqrt{\frac{8 R T}{\pi M}} \quad (3)$$

where m is the mass of the molecule and M is the molar mass. The unit of both masses is Kg in SI. Typical mean speed values are shown in Tab. 4.

Table 4: Mean speed of gas molecules of different mass at room temperature and boiling helium point

| | H₂ | He | CH₄ | N₂ | Ar |
|---|----------------------|-----------|-----------------------|----------------------|-----------|
| $\langle v \rangle$ at 293 K $\left[\frac{\text{m}}{\text{s}}\right]$ | 1761 | 1244 | 622 | 470 | 394 |
| $\langle v \rangle$ at 4.3 K $\left[\frac{\text{m}}{\text{s}}\right]$ | 213 | 151 | 75 | 57 | 48 |

Another important result of the Maxwell-Boltzmann theory is the calculation of the molecular impingement rate φ on a surface, i.e. the rate at which gas molecules collide with a unit surface area exposed to the gas. Assuming that the density of molecules all over the volume is uniform, it can be shown [3] that:

$$\varphi = \frac{1}{4}n\langle v \rangle \quad (4)$$

and using Eq. 3 for the mean speed as obtained by the Maxwell-Boltzmann theory:

$$\varphi = \frac{1}{4}n \sqrt{\frac{8 k_B T}{\pi m}} \quad (5)$$

Numerical values in terms of P, T and molar mass are obtained by Eq. 6; some selected values are reported in Tab. 5.

$$\varphi [\text{cm}^{-2}\text{s}^{-1}] = 2.635 \cdot 10^{22} \frac{P [\text{mbar}]}{\sqrt{M[\text{g}]T[\text{K}]}} \quad (6)$$

Table 5: Molecular impingement rates at room temperature for H₂, N₂, and Ar at some selected pressures

| Gas | Pressure [mbar] | Impingement rate [cm⁻²s⁻¹] |
|----------------|------------------------|---|
| H ₂ | 10 ⁻³ | 1.1 10 ¹⁸ |
| | 10 ⁻⁸ | 1.1 10 ¹³ |
| | 10 ⁻¹⁴ | 1.1 10 ⁷ |
| N ₂ | 10 ⁻³ | 2.9 10 ¹⁷ |
| | 10 ⁻⁸ | 2.9 10 ¹² |
| Ar | 10 ⁻³ | 2.4 10 ¹⁷ |
| | 10 ⁻⁸ | 2.4 10 ¹² |

2.2 Mean free path and Knudsen number

In any physically limited vacuum system, molecules collide between each other and with the walls of the vacuum envelope. In the first case, the average length of the molecular path between two points of consecutive collisions, i.e. the mean free path $\bar{\lambda}$, is inversely proportional to the number density $n = \frac{P}{k_B T}$ and the collision cross section σ_c [4], as given by Eq. 7.

$$\bar{\lambda} = \frac{1}{\sqrt{2} n \sigma_c} \quad (7)$$

For elastic collisions between hard spheres, Eq. 7 can be written in terms of the molecular diameter δ :

$$\bar{\lambda} = \frac{1}{\sqrt{2} \pi n \delta^2} = \frac{k_B T}{\sqrt{2} \pi P \delta^2} \quad (8)$$

The collision cross sections for common gas species in vacuum systems are listed in Tab. 6.

Table 6: Elastic collision cross sections for five different molecules

| Gas | H ₂ | He | N ₂ | O ₂ | CO ₂ |
|-------------------|----------------|------|----------------|----------------|-----------------|
| $\sigma_c [nm^2]$ | 0.27 | 0.27 | 0.43 | 0.40 | 0.52 |

For numerical purpose, Eq. 8 can be rewritten for a specific gas as a function of temperature and pressure. For example, for H₂:

$$\bar{\lambda}_{H_2} [m] = 4.3 \cdot 10^{-5} \frac{T[K]}{P[Pa]} \quad (9)$$

The values of the mean free path for H₂ at room temperature are shown in Fig.1 as a function of the gas pressure.

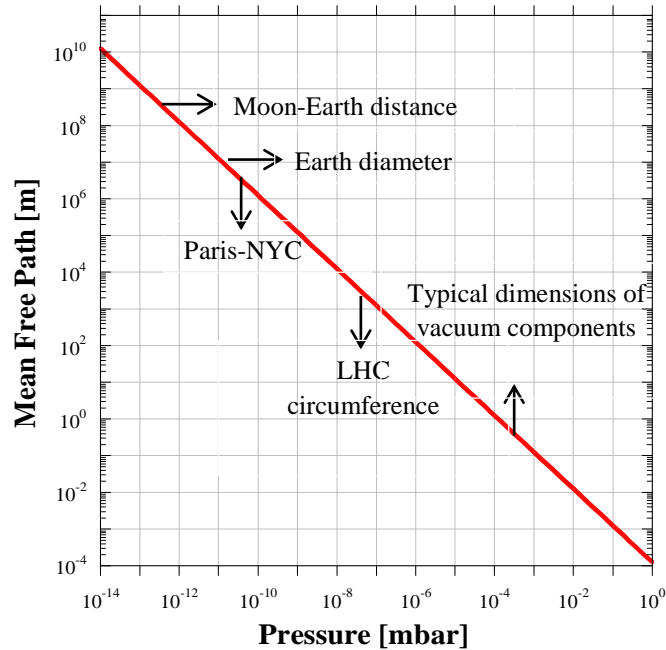


Fig. 1: Mean free path of H₂ molecules at 293 K

When the mean free path is of the order of typical dimensions of the vacuum vessel, for example the diameter of cylindrical beam pipes, molecular collisions with the wall of the vacuum envelope become preponderant. For even longer $\bar{\lambda}$, the gas dynamics is dominated by molecule-wall collisions; intermolecular interactions lose any effect on the gas displacement.

The adimensional Knudsen number K_n translates into numerical values the considerations expressed here above. It is defined as the ratio between the mean free path and a characteristic dimension of a vacuum system (D).

$$K_n = \frac{\bar{\lambda}}{D} \quad (10)$$

The values of K_n delimit three gas dynamic regimes as reported in Tab. 7.

Table 7: Gas dynamic regimes defined by the Knudsen number

| K_n range | Regime | Description |
|-------------------------------|---------------------------|--|
| $K_n > 0.5$ | Free molecular flow | Molecule-wall collisions dominate |
| $K_n < 0.01$ | Continuous (viscous) flow | Gas dynamic dominated by intermolecular collisions |
| $0.5 < K_n < 0.01$ | Transitional flow | Transition between molecular and viscous flow |

Typical beam pipe diameters are of the order of 10 cm. Therefore, free molecular regime is obtained for pressure in the low 10^{-3} mbar range or lower. Except for ion source's plasma chambers, vacuum systems of accelerators operate in free molecular regime; only this vacuum regime is considered in this lesson. Excellent introductions to vacuum systems in viscous and transitional regime can be found in Ref. [5] and [6].

The free molecular flow regime characterizes and determines the pumping and pressure reading mechanisms that can be used in particle accelerators. Pumps and instruments must act on single molecules since there is no interaction between molecules. Collective phenomena like pressure waves and suction do not influence gas dynamics in free molecular flow.

2.3 Conductance in free molecular flow

In free molecular regime, the net gas flow Q between two points of a vacuum system is proportional to the pressure difference ($P_1 - P_2$) at the same points:

$$Q = C (P_1 - P_2) \quad (11)$$

C is called the gas conductance of the vacuum system between the two points. In free molecular regime, the conductance does not depend on pressure. It depends only on the mean molecular speed and vacuum system geometry. The conductance is reported as volume per unit time, i.e. $\ell \text{ s}^{-1}$ or $\text{m}^3 \text{ s}^{-1}$.

The conductance is easily calculated for the simplest geometry, i.e. a small wall slot of surface area A and infinitesimal thickness dividing two volumes of the same vacuum system (see Fig. 2).

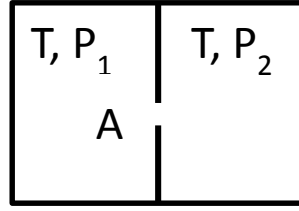


Fig. 2 Schematic drawing of two volumes communicating through a thin and small wall slot

The net flow of molecules from one volume to the other may be calculated by the molecular impingement rate given by the Eq. 4. The number of molecules of volume 1 that go into volume 2 ($\varphi_{1 \rightarrow 2}$) is:

$$\varphi_{1 \rightarrow 2} = \frac{1}{4} A n_1 \langle v \rangle$$

while that from volume 2 to volume 1 are:

$$\varphi_{2 \rightarrow 1} = \frac{1}{4} A n_2 \langle v \rangle$$

The net molecular flow is given by the difference of the two contributions:

$$\varphi_{1 \rightarrow 2} - \varphi_{2 \rightarrow 1} = \frac{1}{4} A (n_1 - n_2) \langle v \rangle$$

and from Eq. 2 and 3:

$$\varphi_{1 \rightarrow 2} - \varphi_{2 \rightarrow 1} = \frac{1}{4} A \frac{\langle v \rangle}{k_B T} (P_1 - P_2)$$

Multiplying both terms of the equality by $k_B T$ and applying Eq. 2, the gas flow in pressure-volume units is obtained:

$$Q = \frac{1}{4} A \langle v \rangle (P_1 - P_2) \quad (12)$$

Comparing Eq. 11 and 12, it comes out that the conductance of the wall slot is proportional to the surface area of the slot and the mean speed of the molecules:

$$C = \frac{1}{4} A \langle v \rangle \propto \sqrt{\frac{T}{m}} \quad (13)$$

From Eq. 3 and 13, it comes out that the conductance of the wall slots is inversely proportional to the square root of the molecular mass. Therefore, for equal pressure drop the gas flow of H_2 is the highest. Finally, for gas molecules of different masses, the conductance scales as the square root of the inverse mass ratio:

$$\frac{C_1}{C_2} = \sqrt{\frac{m_2}{m_1}} \quad (14)$$

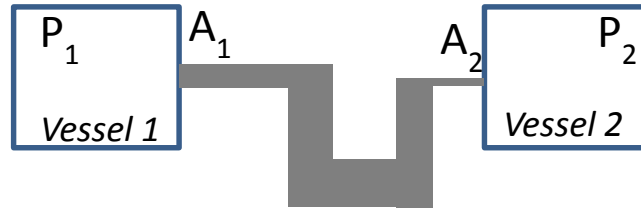
As an example, the conductance for N_2 is $\sqrt{\frac{2}{28}} = 0.27$ times that for H_2 , namely 3.7 times lower. Table 8 collects conductance values, for an orifice, **per unit surface area (C')** at room temperature for common gas species.

Table 8: Unit surface area conductances for common gas species in two different units

| Gas | H ₂ | He | CH ₄ | H ₂ O | N ₂ | Ar |
|---|----------------|------|-----------------|------------------|----------------|------|
| $C' \text{ at } 293 \text{ K} \left[\frac{\text{m}^3}{\text{s m}^2} \right]$ | 440.25 | 311 | 155.5 | 146.7 | 117.5 | 98.5 |
| $C' \text{ at } 293 \text{ K} \left[\frac{\text{l}}{\text{s cm}^2} \right]$ | 44 | 31.1 | 15.5 | 14.7 | 11.75 | 9.85 |

For more complex geometries than wall slots, the transmission probability τ is introduced. If two vessels, at the same temperature, are connected by a duct (see Fig. 3 for symbols), the gas flow from vessel 1 to vessel 2 ($\varphi_{1 \rightarrow 2}$) is calculated multiplying the number of molecules impinging on the entrance section of the duct by the probability $\tau_{1 \rightarrow 2}$ for a molecule to be transmitted into vessel 2 without coming back to vessel 1:

$$\varphi_{1 \rightarrow 2} = \frac{1}{4} A_1 n_1 \langle v \rangle \tau_{1 \rightarrow 2} \quad (15)$$

**Fig. 3:** Schematic drawing of two vessels connected by a duct

Similarly, the gas flow from vessel 2 to vessel 1 is written as:

$$\varphi_{2 \rightarrow 1} = \frac{1}{4} A_2 n_2 \langle v \rangle \tau_{2 \rightarrow 1} \quad (16)$$

In absence of net flow, $\varphi_{1 \rightarrow 2} = \varphi_{2 \rightarrow 1}$ and $n_1 = n_2$, then:

$$A_1 \tau_{1 \rightarrow 2} = A_2 \tau_{2 \rightarrow 1} \quad (17)$$

When $n_1 \neq n_2$ a net flow is set up. It can be calculated by taking into account Eq. 15-17 and 2:

$$\varphi_{1 \rightarrow 2} - \varphi_{2 \rightarrow 1} = \frac{1}{4} A_1 \langle v \rangle \tau_{1 \rightarrow 2} \frac{(P_1 - P_2)}{k_B T} \quad (18)$$

In pressure-volume units, Eq. 18 becomes:

$$Q = \frac{1}{4} A_1 \langle v \rangle \tau_{1 \rightarrow 2} (P_1 - P_2) = C' A_1 \tau_{1 \rightarrow 2} (P_1 - P_2) \quad (19)$$

where, as already mentioned, C' is the conductance of the unit surface area wall slot. Comparing Eq. 11 and 19, it comes out that the conductance of the connecting duct is equal to the conductance of the duct entrance in vessel 1, considered as a wall slot, multiplied by the molecular transmission probability from vessel 1 to vessel 2:

$$C = C' A_1 \tau_{1 \rightarrow 2} \quad (20)$$

2.3.1 Evaluation of the transmission probability

The transmission probabilities depend only on the geometry of the vacuum components. They may be calculated analytically for simple geometry by means of relatively complex integral equations (Clausing equations, see Ref. [7]). Approximate formulas are reported in many vacuum-technology books, for example in Ref. [8].

For the very common case of tubes of uniform circular cross section of length L and radius R , the Santeler equation [9] gives transmission probability with less than 0.7% error.

$$\tau = \tau_{1 \rightarrow 2} = \tau_{2 \rightarrow 1} = \frac{1}{1 + \frac{3L}{8R} \left(1 + \frac{1}{3 \left(1 + \frac{L}{7R} \right)} \right)} \quad (21)$$

For long tubes, i. e. $\frac{L}{R} \gg 1$, Eq. 21 can be simplified :

$$\tau \approx \frac{1}{1 + \frac{3L}{8R}} \approx \frac{8R}{3L} \quad (22)$$

Eq. 22 combined with Eq. 20 gives the conductance of long circular pipes; it is one of the most used equations in vacuum technology. For N_2 it may be written as:

$$C \approx 11.75 \times \frac{\pi D^2}{4} \times \frac{4D}{3L} = 12.3 \frac{D^3}{L} \left[\frac{l}{s} \right] \quad ([D] \text{ and } [l] = \text{cm}) \quad (23)$$

As a result, the conductance of a tube is strongly dependent on its diameter.

The Santeler equation and its approximation for long tubes are plotted in Fig.4. The latter can be applied with errors less than 10% for $\frac{L}{R} \gg 20$. As shown in the same figure, the transmission probability is about 0.5 for circular tubes for which their diameter is equal to their length. In other words, the conductance of such tubes is half that of their entrance surface.

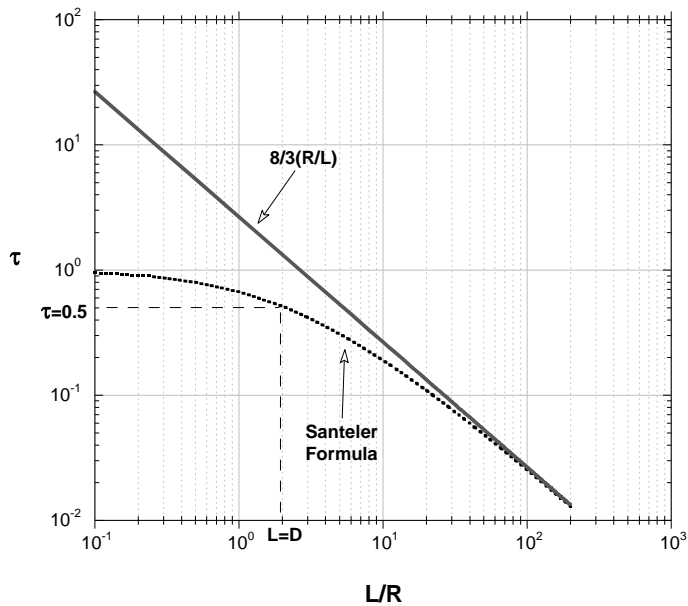


Fig. 4. Transmission probability of tubes of uniform circular cross section calculated by the Santeler equation and its approximation for high L/R

Conductances of more complicated components are calculated by Test-Particle Monte Carlo methods (TPMC). The components are modelled in three dimensions; the TPMC codes generate molecules at the entrance of the component pointing in ‘random’ directions according to the cosine distribution. When the molecules impinge on the internal wall of the component, they are re-emitted again randomly. The programme follows the molecular traces until they reach the exit of the component. The transmission probability is given by the ratio between the number of ‘escaped’ and ‘injected’ molecules [10]. Many simulated molecules are needed to reduce the statistical scattering.

The reference TPMC software at CERN is MolFlow+ [11]. This powerful tool for high-vacuum applications imports the 3-D drawing of the vacuum components and generates ‘random’ molecules on any surface of interest. Fig. 5 shows the model and the molecular tracks for the extraction chamber of the Linac4’s ion source.

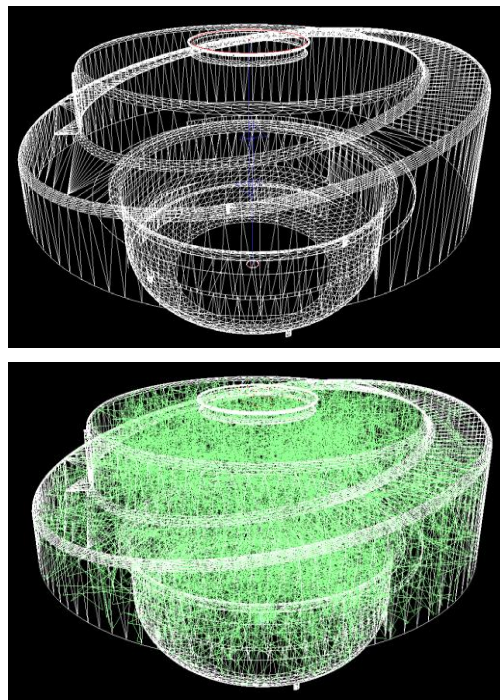


Fig. 5: Meshes used for the Monte Carlo simulation of the extraction chamber of Linac4. The second picture shows molecular tracks (in green) generated by the MolFlow+ code.

2.3.2 Combination of conductances

Elementary vacuum components are installed either in series, i.e. traversed by the same net gas flow, or in parallel, i.e. equal pressures at the extremities.

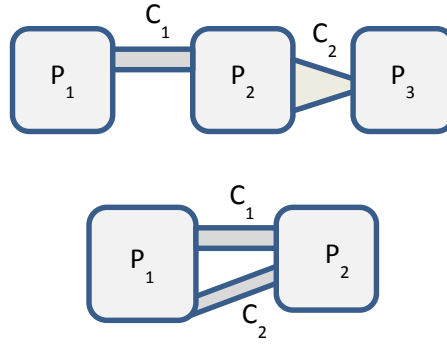


Fig. 6: Schematic drawings of components installed in series (top) and in parallel (bottom).

With reference to Fig. 6, the net gas flow in the two components connected in series is given by the following equations:

$$\begin{aligned} Q &= C_1(P_1 - P_2) \\ Q &= C_2(P_2 - P_3) \end{aligned} \quad (24)$$

A total conductance C_{TOT} equivalent to C_1 and C_2 is introduced in a way that:

$$Q = C_{TOT}(P_1 - P_3) \quad (25)$$

Combining Eq. 24 and 25, C_{TOT} is easily calculated:

$$\frac{1}{C_{TOT}} = \frac{1}{C_1} + \frac{1}{C_2} \quad (26)$$

In general, for N components in series:

$$\frac{1}{C_{TOT}} = \sum_{i=1}^N \frac{1}{C_i} \quad (27)$$

In the same way, it can be shown that for N components installed in parallel the total conductance is the sum of the conductances of all components:

$$C_{TOT} = \sum_{i=1}^N C_i \quad (28)$$

2.4 Pumping speed

In vacuum technology, a pump is any ‘object’ that removes gas molecules from the gas phase. A vacuum pump is characterised by its pumping speed S , which is defined as the ratio between the pumped gas flow Q_P (pump throughput) and the pump-inlet pressure P .

$$S = \frac{Q_P}{P} \quad (29)$$

The pumping speed unit is volume over time, thus the same unit as conductance. In high vacuum, S is in general expressed in $\ell \text{ s}^{-1}$ or $\text{m}^3 \text{ s}^{-1}$; in low and medium vacuum, $\text{m}^3 \text{ min}^{-1}$ is used. In a more general way, S can be defined as the derivative of the pump throughput with respect to the pump inlet pressure

$$S = \frac{\partial Q_P}{\partial P} \quad (30)$$

The pump throughput can be written as the gas flow φ through the cross section of the pump inlet (surface area A_P) multiplied by the capture probability σ , i.e. the probability for a molecule that enters the pump to be definitely removed and never more reappear in the gas phase of the vacuum system (see Eq. 31). In the literature, σ is also called the Ho coefficient.

$$Q_P = \varphi A_P \sigma = \frac{1}{4} A_P n \langle v \rangle \sigma \quad (31)$$

Considering Eq. 13 and 2, it comes out that:

$$Q_P = A_P C' n \sigma = A_P C' \sigma \frac{P}{k_B T}$$

From the definition of pumping speed and converting the throughput in pressure-volume units:

$$S = A_P C' \sigma \quad (32)$$

Therefore, the pumping speed is equal to the conductance of the pump inlet cross section multiplied by the capture probability. The maximum theoretical pumping speed of any pump is obtained for $\sigma=1$ and it is equal to the conductance of the pump-inlet cross section. Tab. 9 reports some values of the maximum pumping speed of lump pumps for typical diameters of the pump inlet. Because S depends on C' , and so on the inverse of the square root of the molecular mass, the maximum theoretical pumping speed is that for H_2 .

Table 9: Maximum pumping speeds in $\ell \text{ s}^{-1}$ for different diameters of circular pump inlets

| ID [mm] | H ₂ | N ₂ | Ar |
|---------|----------------|----------------|------|
| 36 | 448 | 120 | 100 |
| 63 | 1371 | 367 | 307 |
| 100 | 3456 | 924 | 773 |
| 150 | 7775 | 2079 | 1739 |

The pumping speed given by the suppliers is called *nominal pumping speed*; it refers to the pump inlet. The *effective pumping speed* S_{eff} is that acting directly in the vacuum vessel of interest. The effective pumping speed is lower than the nominal due to gas flow restrictions interposed between the pump and the vessel.

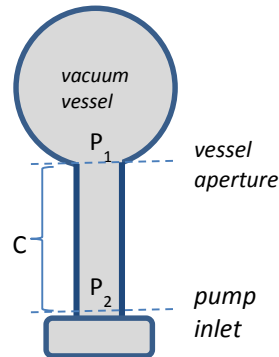


Fig. 7: Schematic drawing of a gas flow restriction of conductance C interposed between a pump of pumping speed S and a vacuum vessel

The effective pumping speed is calculated considering the gas flow from the vessel and the pump. Taking into account Eq. 11 and 29, with reference to Fig. 7:

$$Q = C_1(P_1 - P_2) = SP_2 = S_{eff}P_1$$

and so:

$$\frac{1}{S_{eff}} = \frac{1}{S} + \frac{1}{C} \quad (33)$$

As a result, for $C \ll S$, $S_{eff} \approx C$. In other words, the effective pumping speed does not depend on the installed pump if the conductance of the interposed connection is very low. This conclusion is of primary importance in the design of efficient vacuum systems.

3 Calculation of pressure profiles

The calculation of the pressure profile along vacuum systems is an essential task of vacuum experts and should be tackled at the design phase. In general, the contributions to the total pressure of localized and distributed gas sources are considered separately and finally added. This is possible because in most of the cases the equations that describe pressure profiles are linear. This may be not true if the pumping speed is pressure dependent.

3.1 Pressure profiles generated by localized gas sources

The pressure in a vacuum vessel is obtained by taking into account Eq. 29 and the intrinsic pressure limitation P_0 of the installed pumping system:

$$P = \frac{Q}{S} + P_0 \quad (35)$$

The pumping speed S is either given by the supplier or preliminarily measured. P_0 is the pressure attained in the system without any gas load. When a restriction of conductance C is interposed between the pump and the vessel, the effective pumping speed S_{eff} is considered and Eq. 35 becomes:

$$P = \frac{Q}{S_{eff}} + P_0 = \frac{Q(C + S)}{C \times S} + P_0 \quad (36)$$

When many vessels are interconnected, in each vessel the flow balance is written (node analysis). This analysis leads to a system of linear equations from which the pressure values in each vessel are calculated. As an example, with reference to Fig. 8, in the first vessel, the injected gas flow (Q) is either pumped (P_1S_1) or transmitted to the second vessel ($C_1(P_1-P_2)$). This latter flow is pumped in the second vessel or transmitted in the third vessel, and so on.

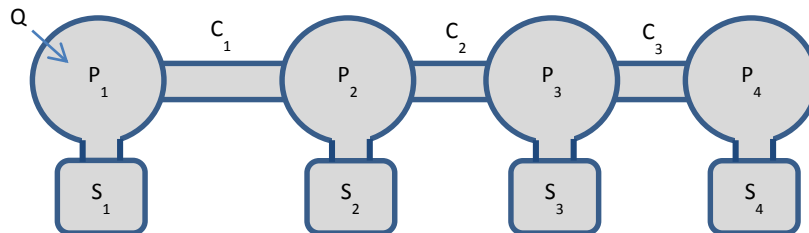


Fig. 8: Schematic drawing of four interconnected vacuum vessels. In each vessel, the gas flow balance is written (node analysis)

$$\begin{aligned}
Q &= P_1 S_1 + C_1(P_1 - P_2) \\
C_1(P_1 - P_2) &= C_2(P_2 - P_3) + P_2 S_2 \\
C_2(P_2 - P_3) &= C_3(P_3 - P_4) + P_3 S_3 \\
C_3(P_3 - P_4) &= P_4 S_4
\end{aligned} \tag{37}$$

When a second localised gas flow is settled, the node analysis is repeated. The contributions of each localised gas flow to the pressure values are then added. If the cross section of the interconnection ducts is constant, it can be shown that the pressure varies linearly between two connected vessels.

3.2 Pressure profiles generated by distributed gas sources

The pressure profiles generated by uniformly distributed outgassing and lump pumps is calculated analytically for simple geometries. Let us consider the case of a cylindrical beam pipe (radius R, length L) connected to a pump at one of its extremities. The calculation starts by imposing a mass balance equation in a generic small fraction of the beam pipe (see Fig. 9):

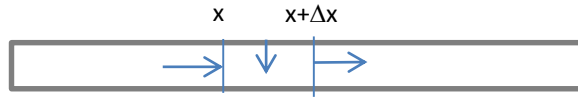


Fig.9: Schematic geometrical model used to write the mass balance equation

$$\begin{aligned}
Q(x + \Delta x) - Q(x) &= 2\pi R \Delta x \cdot q \rightarrow \frac{dQ}{dx} = 2\pi R \cdot q \\
Q(x + \Delta x) &= -C \frac{L}{\Delta x} (P(x + \Delta x) - P(x)) = -CL \frac{\Delta P}{\Delta x} \rightarrow Q(x) = -CL \frac{dP}{dx} \\
\rightarrow CL \frac{d^2 P}{dx^2} &= -2\pi R \cdot q
\end{aligned} \tag{38}$$

Where: q is the outgassing rate of the unit surface area; C, CL and CL/Δx are the beam pipe, the unit length and the section Δx conductances of the beam pipe, respectively.

Eq. 38 indicates that the pressure profile is parabolic. The analytical expression is obtained imposing the pressure at the pump location P(0) and the absence of pressure gradient at the opposite beam pipe extremity (see Fig. 10).

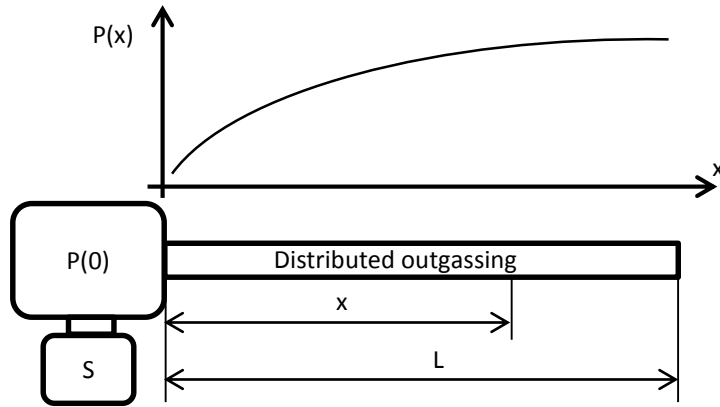


Fig. 10: Pressure profile in a tube pumped at one extremity with uniformly distributed outgassing rate

$$P(0) = \frac{Q_{TOT}}{S} = \frac{2\pi RL \cdot q}{S}$$

$$\left(\frac{dP}{dx}\right)_{x=L} = 0$$

Therefore:

$$P(x) - P(0) = -\frac{Q_{TOT}}{C} \left[\left(\frac{x}{L}\right) - \frac{1}{2} \left(\frac{x}{L}\right)^2 \right] \quad (39)$$

$$P(L) - P(0) = \frac{Q_{TOT}}{2C}$$

Q_{TOT} is the outgassing rate of the whole beam pipe.

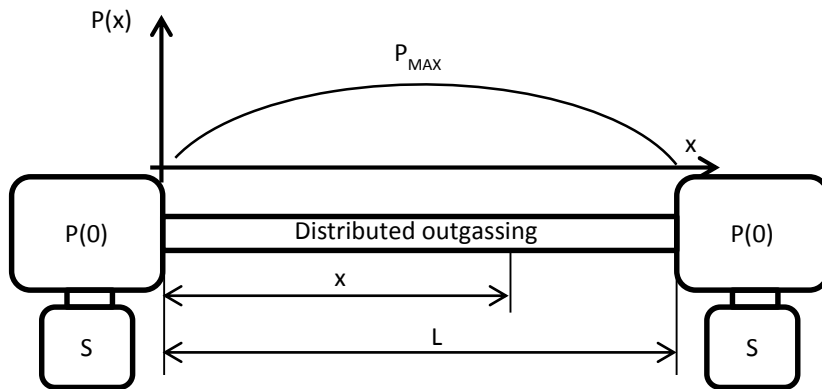


Fig. 11 : Pressure profile in a tube pumped at both extremities with uniformly distributed outgassing rate

If a second identical pump is installed on the other extremity of the beam pipe (see Fig. 11), the pressure profile is again parabolic with a maximum at the centre of the vacuum chamber ($x = L/2$):

$$\begin{aligned}
P(0) &= \frac{2\pi RL \cdot q}{2S} = \frac{Q_{TOT}}{2S} \\
P(x) - P(0) &= -\frac{Q_{TOT}}{2C} \left[\left(\frac{x}{L}\right) - \left(\frac{x}{L}\right)^2 \right] \\
P\left(\frac{L}{2}\right) - P(0) &= \frac{Q_{TOT}}{8C}
\end{aligned} \tag{40}$$

Numerical codes and Monte Carlo simulation are available for geometries that are more complex. Dedicated codes have been extensively used [14].

3.3 Time-dependent pressure profiles

The calculations shown in the previous chapter are valid only for time independent conditions. In time dependent conditions, the variation of the quantity of gas in the vacuum system has to be added to the balance equations such those of Eq. 38. For the simplest vacuum system (vessel and pump), the gas balance equation becomes:

$$\frac{dN}{dt} = Q - SP$$

where Q is the gas load, SP is the gas removed by the pump, and N is the number of molecules in the vacuum system. Differentiating Eq. 2 and converting to pressure-volume units, the following equation is obtained:

$$V \frac{dP}{dt} = Q - SP \tag{41}$$

Eq. 41 is easily solved:

$$P(t) = Ae^{-\frac{t}{\tau_p}} + \frac{Q}{S}$$

The characteristic time of pumping $\tau_p = V/S$ characterises all pressure transient in a vacuum system. The integration constant A is calculated imposing the pressure at $t = 0$. An exponential pressure variation is obtained attaining the stationary value asymptotically. The pressure variation for $P(0)=P_0$ and $P(0)=0$ are shown here below:

$$P(0) = P_0 \rightarrow P(t) = \left(P_0 - \frac{Q}{S}\right) e^{-\frac{t}{\tau_p}} + \frac{Q}{S} \tag{42}$$

$$P(0) = 0 \rightarrow P(t) = \frac{Q}{S} \left(1 - e^{-\frac{t}{\tau_p}}\right) \tag{43}$$

In case of time-dependent gas sources, as in pulsed ion sources, the solution of Eq. 41 is given by:






$$P(t) = \frac{\int e^{\frac{t}{\tau_p}} \frac{Q_{in}(t)}{V} dt + A}{e^{\frac{t}{\tau_p}}} = \frac{\int Q_{in}(t) dt}{V} - \frac{e^{-\frac{t}{\tau_p}}}{V\tau_p} \int \left[\int Q_{in}(t) dt \right] dt + Ae^{-\frac{t}{\tau_p}} \quad (44)$$

For complex vacuum systems where several components are interconnected, the balance equation (Eq. 41) is written for each vessel. This results in a system of coupled differential equations whose solution could be time-consuming. However, the analogy between vacuum systems and electrical networks may be used to accelerate the calculation.

3.4 Calculation of pressure profiles by the electrical analogy

Eq. 11, 26, and 27 show that there is an analogy between vacuum systems and electrical networks. In Tab. 11 vacuum components and variables are correlated with electrical elements and characteristics.

Table 11: Electrical analogy of vacuum components and variable

| Vacuum element | Electrical elements | Electrical symbol |
|--------------------------|-----------------------|---|
| Conductance C | Conductance 1/R |  |
| Gas Flow Q | Current I | |
| Pressure P | Voltage V | |
| Volume V | Capacitance C |  |
| Pump | Conductance to ground |  |
| Gas source | Current generator |  |
| Constant pressure source | Voltage supply |  |

The ground potential is equivalent to zero pressure. A vacuum chamber of a given conductance and volume corresponds to two resistances and a capacitance. For symmetry, the capacitance is placed in the middle of the two resistances. If a local gas source and a pump are added, a current generator and a resistance to ground are connected to the circuit (see Fig. 12).

Another typical example is given in Fig. 13; it represents a differential pumping. This configuration is used when a high gas flow must be prevented from reaching the low-pressure side of a vacuum system. It consists of a small diaphragm with pumps on both sides.

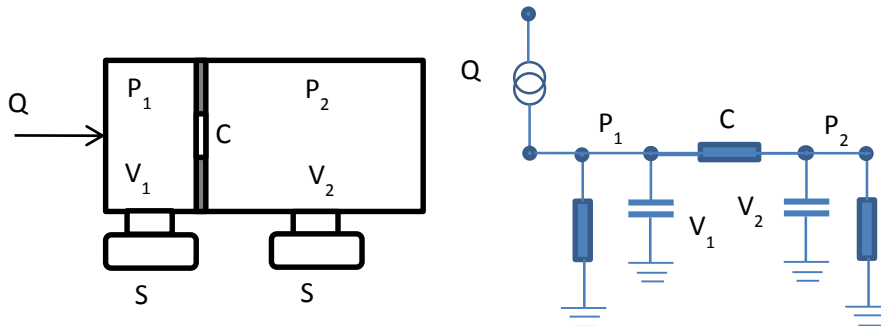


Fig. 13: Electrical analogy of a vacuum system with differential pumping.

Long beam pipes are subdivided into small units to calculate the axial pressure distribution; the small units are considered as single vacuum chambers (volume and conductance) in series. The conductance of a single small unit is equal to the conductance of the entire vacuum chamber times the number of units. Distributed outgassing is taken into account by inserting a current generator on each unit.

The electrical network is solved by dedicated software, for example LTSpice. The time evolution and pulsed sources are easily included in the calculation. Non-linear electric components are used to simulate pressure and time dependent conductances and pumping speeds.

The MedAustron ring [15] and the Linac4 ion source [16] have been fully simulated by means of the electrical analogy. The effects of modifications in the shape of the components, position and size of the pumps have been checked and optimized.

4 Gas sources in particle accelerators

Several gas sources contribute to the total gas load in a vacuum system. Intentional gas injections may be the main source of gas in beam-gas interaction monitors and ion sources. Air leaks due to loss of tightness of components, welds and gaskets can be eliminated by an appropriate design and choice of materials. Air trapped in porosity is minimized by following fundamental guidelines during design, machining and assembling. Permeation of atmospheric gas is negligible whenever all-metal vacuum systems are used.

However, the release of molecules from materials represents an inevitable and, in most of the cases, the dominant source of gas. Gas molecules are adsorbed onto surfaces or dissolved in their bulk [12]. The molecules bound to the surface may be broken if enough energy is available. When the gas removal is spontaneous, i.e. provoked by thermal vibration at standard temperature of the apparatus, the gas release process is called **outgassing**. Gas molecules are also freed by a deliberate action, for example heating at higher temperatures or bombarding the surface with particles (photons, electrons, ions); in this case, the word **degassing** is used. The terms **desorption** and **extraction** are used for the release of molecules adsorbed on the surface and dissolved in the bulk, respectively.

In the family of vacuum materials, polymers and metals have a very different outgassing behaviour (see Tab. 12). The former are prone to dissolve molecules in the voids between the molecular chains, while the latter can dissolve only limited quantities of small atoms that are immobile in the lattice at room temperature, except for hydrogen. For example, in one day, H atoms travel in average 4 μm in austenitic stainless steels while O atoms travel the same distance in 1000 years. Therefore, amongst the dissolved elements in the bulk of metals, only H_2 is released at room temperature. For comparison, in one day, H_2O molecules move about 20 μm in PEEK, a high performance polymer.

Table 12: Relevant characteristics of polymers and metals for vacuum applications

| Materials | Characteristics that determine outgassing |
|------------------|--|
| Polymers | Dissolve entire molecules, for example H_2O , O_2 , CO_2 , solvents, etc. |
| | The solubility in the bulk can be very high in particular for H_2O (up to a few weight percentage) |
| | The dissolved molecules have a relatively high mobility |
| Metals | Only single atoms are dissolved (H, O, C, S, etc.) |
| | The atomic solubility is in general very low at room temperature (typically up to 10^3 at. ppm) |
| | Only H has a significant mobility at room temperature |

4.1 Outgassing of metals

After manufacturing and assembling, the surface of metals is covered by several contaminants. Several surface treatments are available, each aiming at removing a specific set of contaminations. Gross contamination and the sorption layer (hydrocarbons, Cl compound, silicone greases, etc) are removed by solvent and detergent cleaning. Solvent molecules interact with contaminations and transport them away from the surface by diffusion. They are in general quite selective; for example, C_2Cl_4 has a wide spectrum of applications, while HFC has a more restricted action. Detergent molecules are dissolved in water; they are based on aggregate of surfactant (surface acting agent) molecules, called micelle, with hydrophilic and lipophilic extremities; they allow organic molecules and water to combine. Detergents are less selective than solvents. Thick oxide layers (1-10 nm thick) are removed by chemical pickling. The damaged skin of metals –full of dislocations, voids, and impurities- if necessary, is removed by acid etching or electropolishing.

4.1.1 Outgassing of water vapour

After thorough surface treatment, water vapour dominates the outgassing process of metals in vacuum. For smooth metals, the outgassing rate is inversely proportional to the pumping time (t); the empirical relationship of Eq. 45 is in general applied.

$$q_{H_2O} \approx \frac{3 \times 10^{-9} \left[\frac{mbar \cdot l}{s \cdot cm^2} \right]}{t[h]} \quad (45)$$

This equation is valid for all metals used in vacuum system (stainless steel, copper, aluminium, titanium, etc.). It has a strong consequence on the operation of vacuum systems for particle accelerators. A reduction of the outgassing rate and of the pressure by a factor of 10 can be obtained by increasing the pumping time by a factor of 10.

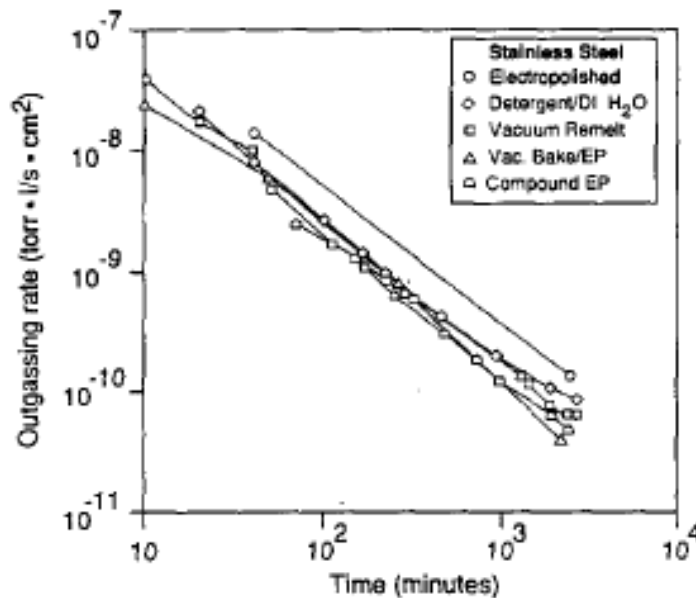


Fig. 14: Water vapour outgassing rate of stainless steel that underwent four different surface treatments [17]

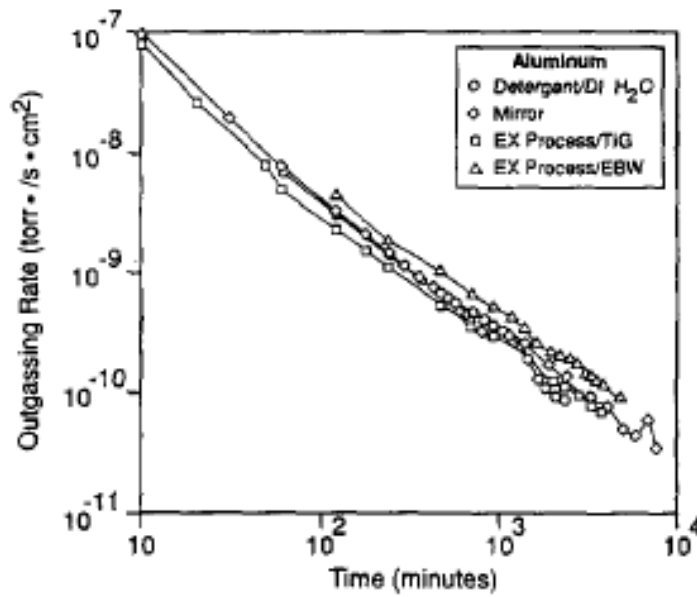


Fig. 15: Water vapour outgassing rate of aluminium that underwent four different surface treatments [17]

The water vapour outgassing rate may be reduced by:

1. Heating in situ during part of the pumpdown time (**bakeout**). The bakeout is very effective for metals if it is carried out for at least 12 h at temperatures higher than 120°C. Water molecules are removed and pumped out faster during the heating time. A much lower pressure is obtained when the system is cooled to room temperature.

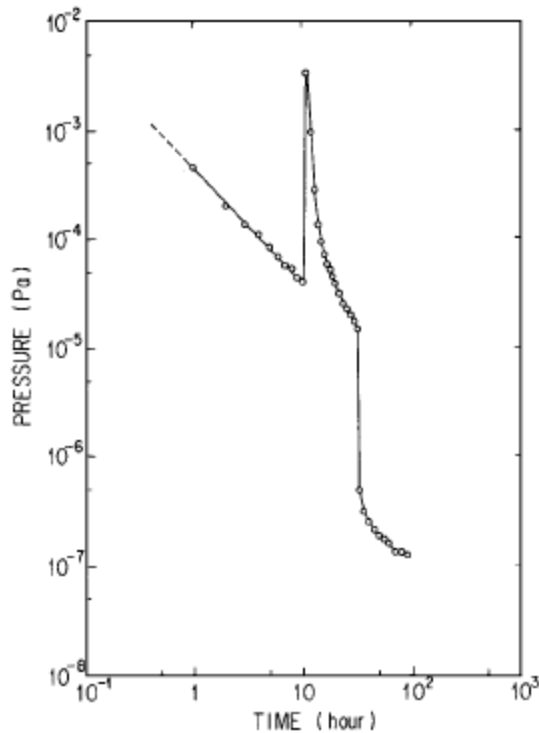


Fig. 16: Pressure evolution in a metallic vacuum system [18]. The pressure peak corresponds to the beginning of the bakeout. The pressure drop follows the system cooling to room temperature

2. Permanently cooling the vacuum system to cryogenic temperature during operation: water molecules remain on the surfaces for a longer time and lower pressures are quickly achieved. In particle accelerators, such a reduction of the outgassing rate is a bonus of cryogenic systems, which aim at attaining superconductivity (for example magnets and RF cavities). The pumping effect of cooling will be developed in chapter 5.

4.1.2 Outgassing of hydrogen

When water vapour outgassing is strongly reduced, by either long pumping or bakeout, the outgassing process is led by H₂. This gas is dissolved in metals as single H atoms. Its diffusion is relatively fast and, after recombination on the surface, it can be released as molecular hydrogen.

Most of the H atoms are dissolved in metals at the liquid state, during the production process. Liquid metals react easily with hydrogenated molecules; moreover H atoms mobility and solubility in the liquid are higher than in the solid. Typical sources of H are:

- metals ores;
- tools needed for fusion;
- refractory materials of furnaces;
- combustion and treatment gas;
- water vapour and fluids used for quenching (for example the hyperquench of austenitic stainless steels is carried out from 1100°C in water, air, or oil).

During the liquid-solid transition, H atoms are trapped in the solid at a concentration much higher than the expected equilibrium value in the solid. Residual hydrogen contents for austenitic stainless steel, copper and aluminium alloys are in the range between 0.1 and 10 ppm in weight. Higher values are reported for very reactive metals like Ti, Nb, and Zr.

Table 13: Typical H₂ outgassing rates after bakeout of metals used in particle accelerators

| Materials | Bakeout | q |
|---------------------------|--------------|--|
| | T[°C] x 24 h | [mbar l s ⁻¹ cm ⁻²] |
| Austenitic st. steel | 150 | 3 10 ⁻¹² |
| Austenitic st. steel | 200 | 2 10 ⁻¹² |
| Austenitic st. steel | 300 | 5 10 ⁻¹³ |
| Copper Silver added (OFS) | 150 | 3 10 ⁻¹² |
| Copper Silver added (OFS) | 200 | ≈ 10 ⁻¹⁴ |
| Beryllium | 150 | < 10 ⁻¹⁴ |
| Al alloys | 150 | < 10 ⁻¹³ |

As for water vapour, hydrogen-outgassing rate is reduced by heating the vacuum components (see Tab. 13). Higher temperatures increase the H atoms mobility and, as a result, accelerate the depletion of the residual hydrogen content. However, there is a crucial difference between water vapour and hydrogen. Each time the vacuum system is exposed to air, water molecules re-adsorb on the surface, while hydrogen is not recharged in the bulk of the metal. H refilling is blocked by the difficult dissociation of the molecule on the native oxide layer. In addition, at room temperature, for most of the materials used for the manufacturing of vacuum chambers the H solubility is very low. For example, to recharge 1 wt. ppm of hydrogen at room temperature in stainless steel, the material has to be in equilibrium with the gas at 7 bar. The hydrogen pressure in air is roughly 10^{-4} mbar, which gives a maximum recharging of about $2 \cdot 10^{-4}$ wt. ppm.

The most important consequence is that vacuum materials may be degassed ex situ in a vacuum furnace. Once in air, the benefit of the degassing treatment is not lost.

For copper and aluminium alloys, a few bakeout at 150-200°C for 24 hours are sufficient to reduce the hydrogen-outgassing rate to less than 10^{-13} mbar $l\ s^{-1}\ cm^{-2}$. For austenitic stainless steel, higher temperatures are needed to have a similar effect for a few mm thick vacuum chambers. Repeated bakeout at temperature higher than 200°C may have a significant influence. There is experimental evidence that the ratio of the hydrogen outgassing rates q measured at room temperature after two successive identical bakeouts is a constant.

$$\frac{q_{n+1}}{q_n} = const. \quad (46)$$

In addition, q depends exponentially on temperature as for an activated process:

$$q = q_0 \exp\left(-\frac{E}{k_B T}\right) \rightarrow \ln \frac{q}{q_0} = -\frac{E}{k_B T} \quad (47)$$

A radical effect is obtained by heating in a vacuum furnace to temperature up to about 1000°C. Such a treatment is called '**vacuum firing**'. At CERN it is carried out at 950°C for 2 h in a vacuum better than 10^{-5} mbar at the highest temperature.



Fig. 16: The CERN's large furnace dedicated to vacuum firing of austenitic stainless steels. Useful height and diameter: 6 m and 1 m, respectively. Maximum charge weight: 1000 Kg. Ultimate pressure: about 10^{-7} mbar; pressure at the end of the 950°Cx2h treatments: 10^{-5} mbar.

4.1.3 The diffusion model of hydrogen outgassing

If hydrogen outgassing is controlled by diffusion of atomic H in the bulk of materials toward the surface, the Fick's laws might predict the measured values. In one dimension, it can be written that:

$$\Gamma(x, t) = -D \frac{\partial c(x, t)}{\partial x} \quad (48)$$

$$\frac{\partial c(x, t)}{\partial t} = D \frac{\partial^2 c(x, t)}{\partial x^2} \quad (49)$$

D is the diffusion coefficient of H atoms in the metals: $D = D_0 e^{-\frac{E_D}{k_B T}}$ and E_d is the diffusion energy.

$c(x, t)$ is the concentration of H atoms in the metal at the position x and time t.

$\Gamma(x, t)$ is the flow of H atoms in the metal at position x and time t.

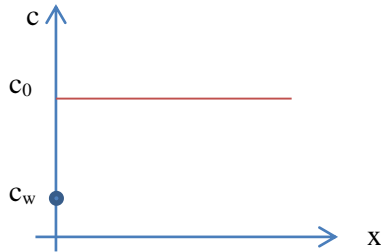
From the first of the two equations, the outgassing rate may be written as:

$$q(t) = -\frac{1}{2} D \frac{\partial c(x_s, t)}{\partial x} \quad (50)$$

x_s being the ordinate of the surface. The 1/2 factor takes into account the facts that two H atoms are needed to form one H_2 molecule.

4.1.3.1 The semi-infinite-solid approximation.

In the **semi-infinite solid approximation**, for initial conditions $c(x, 0) = c_0$ (this is the residual content of hydrogen at the reception of the vacuum material) and a constant concentration on the surface $c(0, t) = c_w$, the concentration and the outgassing rate are:



$$c(x, t) = (c_0 - c_w) \cdot \operatorname{erf}\left(\frac{x}{2\sqrt{Dt}}\right) \quad (51)$$

$$q(t) = \frac{D(c_0 - c_w)}{\sqrt{\pi Dt}} \rightarrow q(t) \propto t^{-0.5} \quad (52)$$

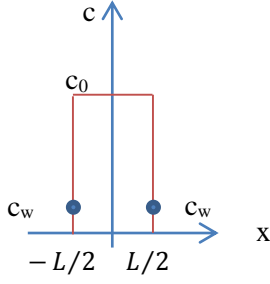
The $t^{-0.5}$ variation of the outgassing rate holds also for slab when the thickness L is much larger than the diffusion length, i.e. \sqrt{Dt} .

4.1.3.2 The slab approximation.

In general for **slab**, the boundary condition is $c\left(\pm \frac{L}{2}, t\right) = c_w$, while the initial condition is always $c(x, 0) = c_0$. In this case, the calculated outgassing rate is:

$$q(t) = \frac{4(c_0 - c_w)}{L} D \sum_{n=0}^{\infty} \exp\left[-(2n+1)^2 \pi^2 \frac{Dt}{L^2}\right] \quad (52)$$

For $Dt > 0.05 L^2$ only the first term of the series is relevant:



$$q \approx \frac{4(c_0 - c_w)}{L} D e^{-\pi^2 \frac{Dt}{L^2}} \quad (53)$$

4.1.3.3 The Sievert's law

If hydrogen in the gas phase and on the surface are in equilibrium, the surface concentration c_w may be calculated by the Sievert's law:

$$c_w = K_s(T) \sqrt{P_{H_2}} \quad (54)$$

$$K_s(T) = K_0 e^{\frac{-E_s}{2k_B T}}$$

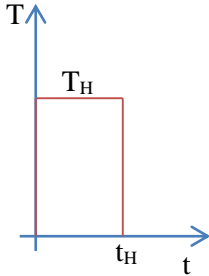
where P_{H_2} is the pressure of hydrogen in the gas phase, $K_s(T)$ is the hydrogen solubility in the metal, E_s is the gas solubility energy, and K_0 a constant. In case of endothermic solution, as in most of the structural material for particle accelerators, E_s is positive; therefore, the solubility increases with temperature. At room temperature and for typical hydrogen pressure, c_w is negligible with respect to the residual hydrogen content. This is not true at higher temperature; for example during a vacuum firing treatment. Eq. 55 gives the Sievert's law for austenitic stainless steel, in different units.

$$c_H [at.ppm] = 71.8 \cdot \sqrt{P_{H_2} [Torr]} \cdot e^{\frac{0.114[eV]}{k_B T}} \quad (55)$$

$$c \left[\frac{Torr \cdot l(H_2)}{cm^3} \right] = 8.21 \cdot 10^{-2} \sqrt{P_{H_2} [Torr]} \cdot e^{\frac{2650}{1.99T[K]}}$$

4.1.3.4 Arbitrary thermal cycle

The Fick's laws (Eq. 48 and 49) can be used to calculate the outgassing rate at room temperature of slabs after arbitrary thermal cycles. In the simplest case, the material is heated at a constant temperature T_H for a duration t_H . After cooling at room temperature T_{RT} , the calculated outgassing rate is:



$$q(t) \approx \frac{4(c_0 - c_w)}{L} D(T_{RT}) \exp \left[-\pi^2 \frac{D(T_H) t_H}{L^2} \right] \quad (56)$$

For an arbitrary temperature profile $T=T(t)$:

$$q(t) \approx \frac{4(c_0 - c_w)}{L} D(T_{RT}) \exp \left[-\pi^2 \frac{\int_0^{t_H} D(T_H(t)) dt}{L^2} \right] \quad (57)$$

For analogy with thermal transmission, the dimensionless number:

$$F_0 = \frac{\int_0^{t_H} D(T_H(t)) dt}{L^2} \quad (58)$$

is called the Fourier number. It is the square of the ratio of the diffusion length to the slab thickness. It indicates how much of the initial residual hydrogen concentration is depleted during the thermal treatment. For $F_0 > 3$, the material can be considered as emptied or in equilibrium with the surrounding gas.

In case of multiple identical thermal treatments (for example bakeouts) at temperature T_H and duration t_H , the calculated ratio of the outgassing rate at room temperature after two successive thermal cycles is:

$$\frac{q_{n+1}}{q_n} = \exp\left[\pi^2 \frac{D(T_H)t_H}{L^2}\right] \quad (59)$$

That is to say that each bakeout reduces the outgassing rate of hydrogen by the same constant factor. This is in line with the experimental results of Eq. 46.

4.1.3.5 The diffusion model of vacuum firing

As already written, vacuum firing aims at removing as much as possible hydrogen from the bulk of materials, notably austenitic stainless steels. The heating temperature is higher than that for the in situ bakeout. At CERN, the standard treatment for austenitic stainless steels is 950°C for 2 hours in a vacuum better than 10^{-5} mbar (mainly H_2).

Table 14: Parameters of the vacuum firing treatments used for the diffusion model

| Parameters | Symbol | Values |
|---|----------|---|
| Temperature of the firing treatment | T_f | 950°C |
| Duration of the firing treatment | t_f | 2 hours |
| In situ bakeout temperature | T_{bo} | 150°C |
| Duration of the in situ bakeout | t_{bo} | 24 hours |
| Initial content of residual hydrogen | c_o | 1 ppm wt (≈ 50 ppm at.) |
| Hydrogen equilibrium concentration on slab surfaces during firing | c_w | 0.06 ppm wt. Equivalent to $P_{H_2} = 1.3 \times 10^{-5}$ mbar |

For vacuum chambers **thinner than 3 mm** such a thermal cycle results in Fourier numbers larger than 3; that is, the residual hydrogen is completely removed and the material reaches equilibrium with the hydrogen in the gas phase in the furnace. The hydrogen pressure during the treatment determines the final hydrogen content in the material (Sievert's law, Eq. 55) and the resulting outgassing rate.

For materials thicker than a few mm, the residual hydrogen is only partially removed and the Fourier number is lower than 3, namely the diffusion length is lower than the thickness of the material ($L > \sqrt{D_H t_H}$). When the slab thickness is much higher than the diffusion length, the semi-infinite solid approximation can be applied. In this case, the outgassing rate does not depend significantly on the hydrogen pressure in the furnace during the treatment because $c_w \ll c_0$ (see Eq. 52).

In real application, after the vacuum firing (T_f, t_f), in situ bakeout is carried out (T_{bo}, t_{bo}) to remove water vapour. The diffusion model may be applied to calculate the resulting hydrogen outgassing rate at room temperature T_{RT} ; Eq. 60 gives the numerical values.

$$q(t) = \frac{4 \cdot c_w \cdot D(T_{RT})}{L} \sum_{n=0}^{\infty} e^{-(2n+1)^2 \pi^2 \cdot F_o(T_{bo}, t_{bo})} + \frac{4 \cdot (c_0 - c_w) \cdot D(T_{RT})}{L} \sum_{n=0}^{\infty} e^{-(2n+1)^2 \pi^2 [F_o(T_f, t_f) + F_o(T_{bo}, t_{bo})]} \quad (60)$$

Fig. 17 shows the outgassing values as a function of the slab thickness for the parameters reported in Tab. 14. The thick and thin slab limits are easily identified; their outgassing rates differ by a factor of about 20. This result is experimentally verified.

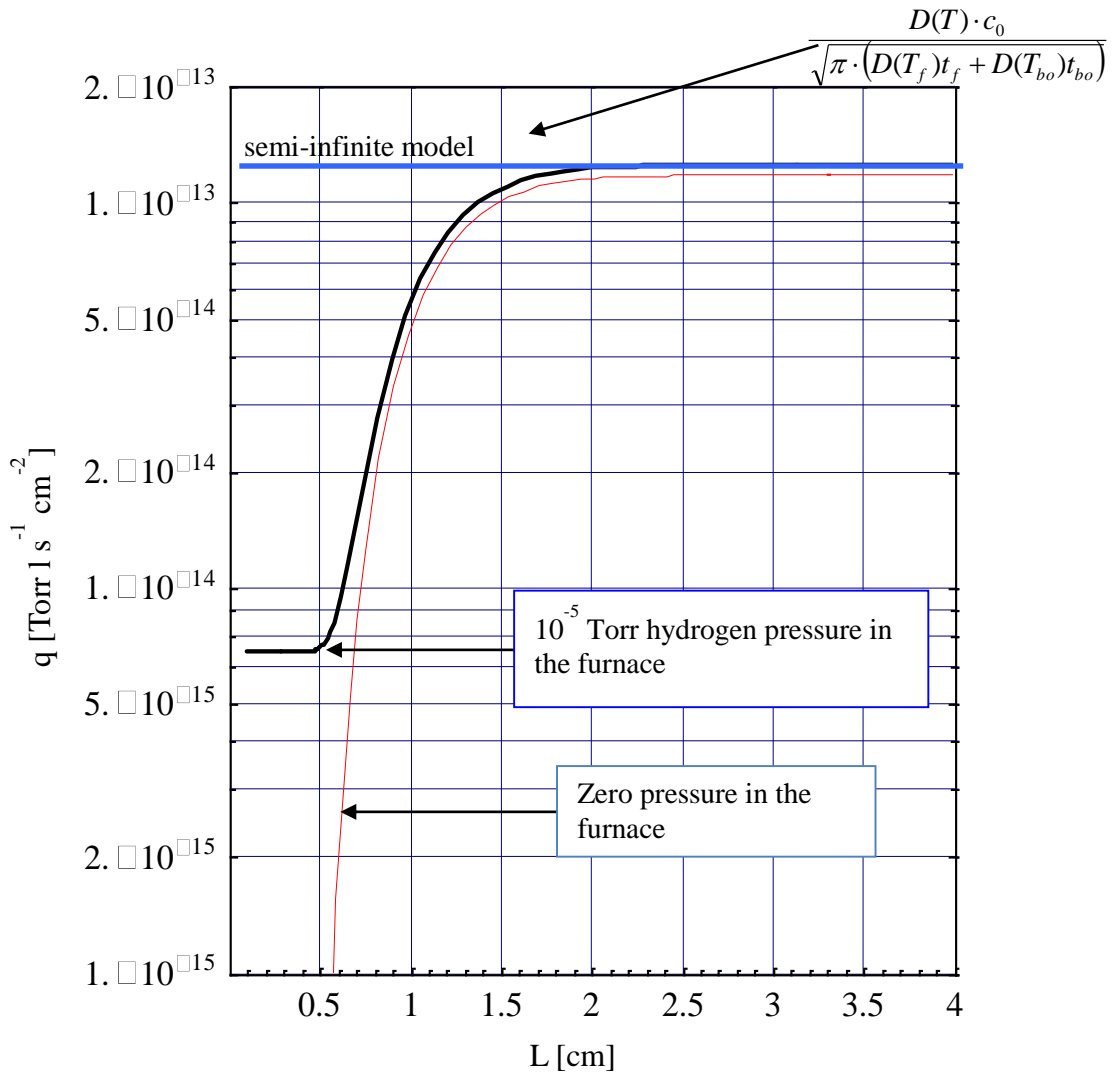


Fig. 17: Hydrogen outgassing rate after vacuum firing (see Tab. 14 for the used parameters)

4.1.4 The air bakeout

The heating of austenitic stainless steels in air or pure oxygen is as effective as vacuum firing to reduce hydrogen outgassing rates. The air bakeout was proposed in the sixties; it was reported to decrease the hydrogen degassing rate at room temperature by three orders of magnitude. Typical heating temperatures are in the range 400-450°C for tens of hours. During heating, the oxide layer growth ten times more than the native oxide; it is mostly composed of iron oxide.

This treatment is not intentionally used for particle accelerators; however, it was applied to the vacuum chambers of the VIRGO gravitational interferometer.

4.2 Outgassing of polymers

Polymers are used for some specific applications in vacuum systems of accelerators: sealing, electrical insulators, supports, etc. In UHV they are never used because of their high outgassing rate, except for valve sealing in particular applications. Their application in high radioactive environment is avoided because radiations generate loss of the mechanical performance, brittleness, and decomposition.

4.2.1 Some notes about polymer structures

Polymers are classified according to morphology in:

- Thermoplastics: soften when heated and return to original condition when cooled.
- Thermosets: solidify or "sets" irreversibly when heated.
- Elastomers: can be stretched to several times their length and rapidly return to their original dimension when the applied stress is released.

The polymer structure has an important influence in gas diffusion and therefore in outgassing. The three different structures are:

- Crystalline: macromolecules form three-dimensionally ordered arrays called **lamella** (plate-like) crystals with a thickness of 10 to 20 nm in which the parallel chains are perpendicular to the face of the crystals.

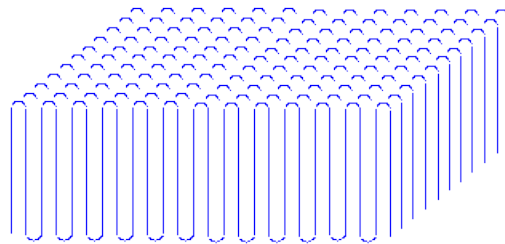


Fig. 18: Schematic view of a polymeric crystalline structure

- Amorphous: no long-range order (spaghetti like material). Amorphous polymers are softer, have lower melting points, and are penetrated by solvents more than are their crystalline counterparts.

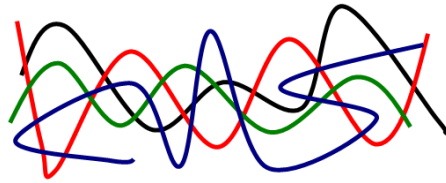


Fig. 19: Spaghetti-like amorphous structure of polymers

- Semicrystalline: mixing of crystalline and amorphous regions; crystals are small and connected to the amorphous regions by polymer chains so there may be no sharp well-defined boundaries between the two types of regions.

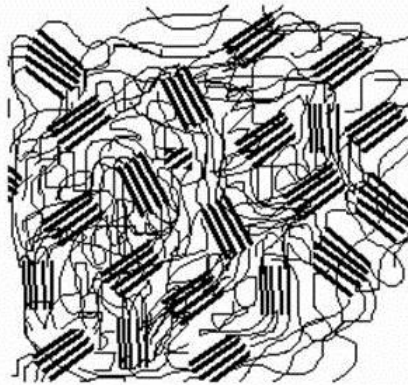


Fig. 20: Semicrystalline structure of polymers.

Copied from <http://web.utk.edu/~mse/Textiles/Polymer%20Crystallinity.htm>

The **amorphous regions** can be either in the glassy or rubbery state. The temperature at which the transition, in the amorphous regions, between the glassy and rubbery state occurs is called the **glass transition temperature T_g** . Below T_g , amorphous polymers are stiff, hard and often brittle; in this state the molecules are frozen on place. This generates stable empty space called excess volume. Above T_g , portions of molecules can start to wiggle around: the polymer is in the **rubbery state**, which provides softness and flexibility.

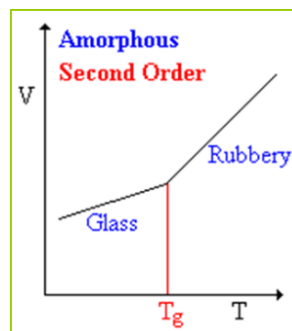


Fig. 21: Glassy-rubbery transition in the amorphous phase of polymers.

Outgassing rates of polymers is known to be much higher than that of metals. Two reasons explain this phenomenon: a polymer contains much more gases than a metal, and the gas mobility in polymers is orders of magnitude larger than in metals.

In the rubbery state the gas molecules are dragged by the thermal movement of the chain. In the glassy state the gas molecules diffuse through the volume of the polymer and also through the excess volume. The diffusion process in amorphous or semicrystalline polymers is not always well described by Fick's law. The diffusion mechanism can be distinguished by evaluating the **Deborah number D_e**

$$D_e = \frac{\tau}{\nu}$$

where τ is the relaxation time of the polymer during the diffusion of a molecule, and $\nu=L^2/D$ is the characteristic time for diffusion. For $D_e \gg 1$ the time for diffusion is shorter than the time for relaxation, the diffusing molecules does not perceive any change in the polymer structure and as a consequence the Fick's law is valid. For $D_e \ll 1$ the penetrating molecules swell the polymer, modify the material structure, and hence allow the adsorption of additional molecules; in this latter situation the diffusion process cannot be described as a fickian process. This is the typical case of H_2O in polymers.

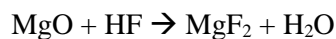
4.2.2 Elastomers

In elastomers the molecular chains are reticulated (formation of 3D networks) by vulcanization. The process of vulcanization was developed by Goodyear and Hancock (1844). It consists in heating natural rubber with sulfur. Chemical bonds are formed by chains of sulfur atoms which react with the unsaturated bonds of the primary macromolecules. Modern elastomers utilize a wide variety of chemicals to produce the permanent network. Fluorocarbon rubbers are prepared by cross linking a copolymer of tetrafluoro-ethylene and hexafluoro-propylene. These rubbers are thermally stable and have very low coefficient of friction. Viton[®] is a fluorocarbon rubber typically employed for O-ring in vacuum technology.

Table 15: Typical elements of the Viton composition [19]

| Components | Parts by wt. |
|--------------------------|--------------|
| Viton [®] resin | 100 |
| Carbon black treatment | 25 |
| MgO | 15 |
| Curing agent | 1.5 |

The MgO is added in Viton[®] as an acid acceptor to remove small amount of HF which results from the curing of the resin. The reaction is:



Therefore, Viton[®] is created with a built-in source of water.

Viton[®] should never be cleaned with solvents, because the solvent is dissolved in the material and its outgassing could affect the vacuum performance for days. Pre-baking of O-ring gaskets at 200°C for some hours in air or vacuum is a necessary operation to remove contaminants remaining from the production.

4.2.3 Outgassing rates of polymers

Polymers, in particular their amorphous structures, can dissolve huge quantities of gas. The water vapour solubility is very high; for example for common materials like Viton, PEEK, and Vespel the content of water in equilibrium with 50% humidity air at 20°C is 0.21, 0.2, and 1 wt. %, respectively. The huge quantity of dissolved gas and the relatively high mobility through the polymeric chains result in much higher outgassing rates than the ones for metals. This is particularly marked for water vapour.

The outgassing rates of polymers reported in the literature have a large spread. This could be due to the large dispersion in the composition and the source of the resin; the different history of the samples; and, for water vapour, the relative humidity of the laboratory as well. Data are available for baked and unbaked polymers, in particular for those used for sealing. The maximum bakeout temperature depends on the type of polymer; it is limited to about 200 °C for Viton®.

Table 16: Outgassing rates (essentially water vapour) of different polymers [19]. The values are reported in Torr l s⁻¹ cm⁻².

| Polymer | Unbaked, 1 h pumping | Baked, ultimate |
|--------------------|--|--|
| Fluoroelastomer | 4 × 10 ⁻⁷ –2 × 10 ⁻⁵ | 3 × 10 ⁻¹¹ –2 × 10 ⁻⁹ |
| Buna-N | 2 × 10 ⁻⁷ –3 × 10 ⁻⁶ | --- |
| Neoprene | 5 × 10 ⁻⁵ –3 × 10 ⁻⁴ | --- |
| Butyl | 2 × 10 ⁻⁶ –1 × 10 ⁻⁵ | --- |
| Polyurethane | 5 × 10 ⁻⁷ | --- |
| Silicone | 3 × 10 ⁻⁶ –2 × 10 ⁻⁵ | --- |
| Perfluoroelastomer | 3 × 10 ⁻⁹ | 3 × 10 ⁻¹¹ –3 × 10 ⁻¹⁰ |
| Teflon | 2 × 10 ⁻⁸ –4 × 10 ⁻⁶ | --- |
| KEL-F | 4 × 10 ⁻⁸ | 3.5 × 10 ⁻¹⁰ |
| Polyimide | 8 × 10 ⁻⁷ | 3 × 10 ⁻¹¹ |

The outgassing rates of thick (L>Dt) slab of polymers are expected to decrease with the inverse of the square root of the pumping time t (see Eq. 52):

$$q_{H_2O} \propto \frac{1}{\sqrt{t}}$$

This means that, compared to unbaked metals, thick polymers experience a much slower reduction of water outgassing rate (see 4.1.1).

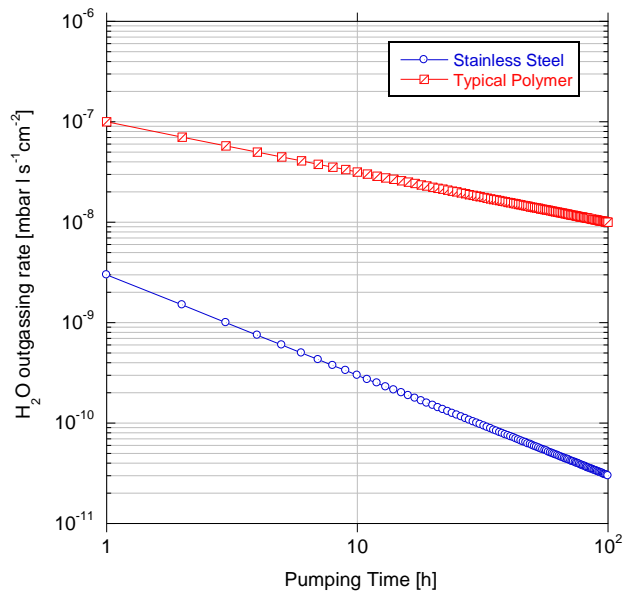


Fig. 22: Water vapour outgassing rates of metals and polymers. The absolute values for the polymer curve are only indicative; they are plotted to give a hint about the different behaviour with respect to metals.

Another important limitation of polymers used as seals is the high gas permeability: atmospheric gas penetrates into the material and diffuses towards the vacuum system. The permeation flow may limit the ultimate water vapour pressure in vacuum systems and affect the sensitivity of helium leak-detection. As an example, the permeation flow of atmospheric water through a Viton O-ring, 5 mm cross section diameter, 6 cm torus diameter, is about 10^{-7} mbar $l s^{-1}$. The stationary condition (ultimate permeation) will be attained after about two months. Values of permeability are listed in Tab. 16.

Table 16: Room temperature (20-30°C) permeability of different molecules in polymers [19]. The values are reported in $scm s^{-1} cm^{-2} cm atm^{-1}$.

TABLE VI. Permeation data for various polymers and gases.^{3,19,47-50} The temperature range is 20°-30°C. The units are $scm s^{-1} cm^{-2} cm atm^{-1}$.

| Polymer | Helium (K × 10 ⁸) | Nitrogen (K × 10 ⁸) | Oxygen (K × 10 ⁸) | Carbon dioxide (K × 10 ⁸) | Water (K × 10 ⁸) |
|-----------------|----------------------------------|------------------------------------|----------------------------------|--|---------------------------------|
| Fluoroelastomer | 9-16 | 0.05-0.3 | 1.0-1.1 | 5.8-6.0 | 40 |
| Buna-N | 5.2-6 | 0.2-2.0 | 0.7-6.0 | 5.7-48 | 760 |
| Buna-S | 18 | 4.8-5 | 13 | 94 | 1800 |
| Neoprene | 10-11 | 0.8-1.2 | 3-4 | 19-20 | 1400 |
| Butyl | 5.2-8 | 0.24-0.35 | 1.0-1.3 | 4-5.2 | 30-150 |
| Polyurethane | — | 0.4-1.1 | 1.1-3.6 | 10-30 | 260-9500 |
| Propyl | — | 7 | 20 | 90 | — |
| Silicone | — | — | 76-460 | 460-2300 | 8000 |
| TEFLON | — | 0.14 | 0.04 | 0.12 | 27 |
| KEL-F | — | 0.004-0.3 | 0.02-0.7 | 0.04-1 | — |
| Polyimide | 1.9 | 0.03 | 0.1 | 0.2 | — |

The permeation flow per cm^2 of exposed surface is calculated from the permeability Π of Tab. 16 by the following formula:

$$q \left[\frac{\text{mbar} \cdot \text{l}}{\text{s}^{-1} \text{cm}^{-2}} \right] \cong 10^{-3} \cdot \left[\frac{\text{mbar} \cdot \text{l}}{\text{cm}^2 \text{s}} \frac{\text{cm}}{\text{mbar}} \right] \cdot \Pi \left[\frac{\text{sccm}^3}{\text{cm}^2 \text{s}} \frac{\text{cm}}{\text{atm}} \right] \cdot \frac{P[\text{mbar}]}{L[\text{cm}]}$$

where L is the thickness of the polymeric gasket (for example, the torus diameter of a gasket) and P the pressure in the atmosphere of the permeating gas (for example 20 mbar of water vapour in air).

4.2.4 Reduction of the outgassing rates of polymers by thin film coating

As shown before, polymers have a limited application in vacuum systems of accelerators because they have huge outgassing and permeability. This drawback has been partially overcome in other technological domains (i.e. packaging) by coating polymers with metals or metal oxides (more recently also with a:C-H). Since the permeability in metals is negligible for all gases, metallic coatings should entirely block the polymer outgassing and permeation. However, experimental results show that only a partial reduction of the gas flow is obtained. This is attributed to defects on the coating (pinholes or scratches) that cause discontinuity on the impermeable layer. Pinholes are produced during the deposition process and they are presumably due to atmospheric dust particles.

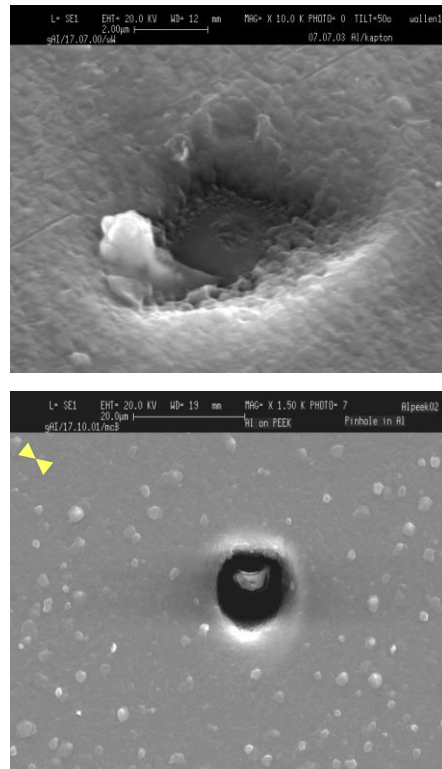


Fig 23: Examples of pinholes on Al coating deposited on PEEK

Transmitted light optical microscopy has confirmed that uncoated surfaces on metal films mainly consist of pinholes of different diameters (see Fig. 24).

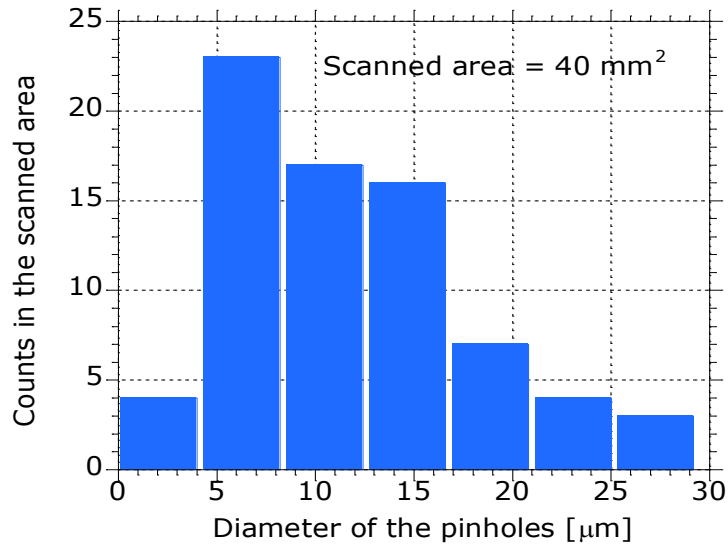


Fig. 24: Distribution of pinholes diameters measured by transmitted light and optical microscopy.

Normalised uncoated surface areas Θ for Al coating deposited on substrate treated in laboratory air are of the order of 10^{-4} ; lower values should be attained if the substrates are treated in clean rooms.

However, experiments have shown that the permeability is reduced much less than expected from the uncoated fraction. For example, for Al coated PEEK (0.125 mm thick), the uncoated fraction is 10^{-4} , but the permeability of He is only 10^{-2} of that of the uncoated polymer.

This apparent inconsistency can be justified considering that the pinhole gas throughput is enhanced by lateral diffusion.

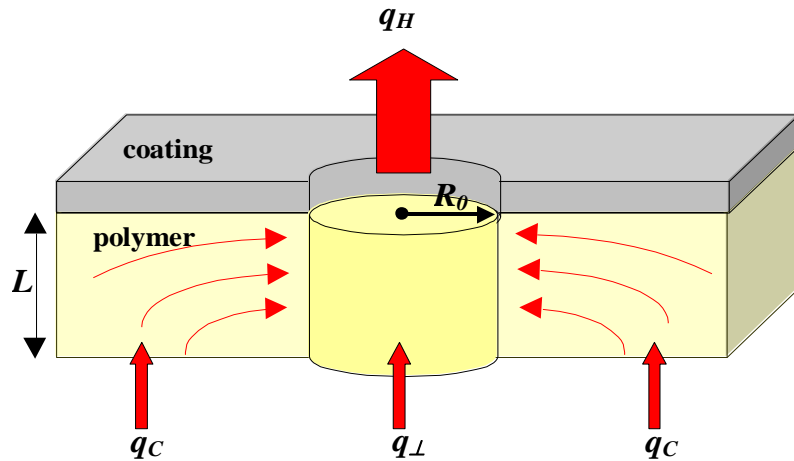


Fig. 25: Pinhole flow (q_H) enhancement due to lateral contribution (q_C) [20].

It can be shown [21] that for $L/R_0 > 0.3$ the normalized permeability ρ , i.e. the ratio of the coated to the uncoated substrate permeabilities, is given by:

$$\rho = \Theta \times \left(1 + 1.18 \frac{L}{R_0} \right) \quad (61)$$

L is the polymer thickness; R_0 is the radius of the pinhole. In the literature the barrier efficiency of the coating is called “barrier improvement factor” or BIF. It is the inverse of normalized permeability.

$$BIF = \frac{1}{\rho} = \frac{1}{\Theta \times \left(1 + 1.18 \frac{L}{R_0}\right)} \quad (62)$$

The improvement due to the coating is less significant for thicker polymer substrates.

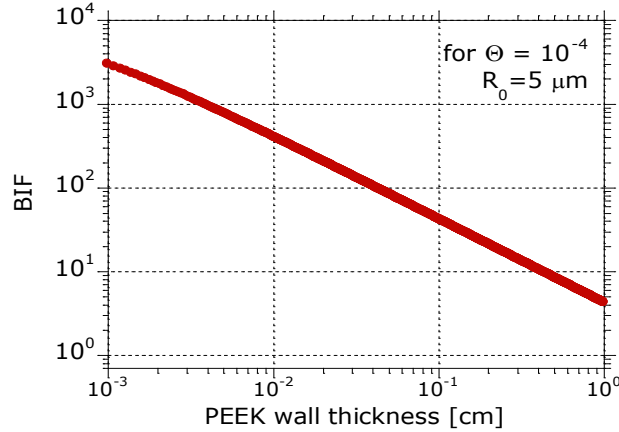


Fig. 26: Barrier improvement factor plotted as a function of the thickness of the substrate (PEEK). The coating is sputtered Al, about 2 μm thick.

In conclusion, metallic coatings are very efficient in the reduction of the permeation and outgassing flow in thin polymers. For polymers thicker than 5 mm, the benefit of the coating is negligible.

4.3 Degassing induced by particle beams

The impingement on solid surfaces of particles (electrons, ions, photons) of energy higher than a few eV may result in desorption of gas molecules and ions. The first observation of electron stimulated desorption was described by Dempster in 1918. In 1909, Millikan was the first to report the evidence of photon induced desorption from data recorded during the measurement of photoelectric current exposed to ultraviolet radiation. The first interpretation is attributed to Winch in 1930. He was the first to understand the implication of photoelectrons in the photon induced desorption. He wrote: ‘The probable explanation is that photoelectrons, both when ejected and returned to the surface by reverse field, remove adsorbed gas from the surface’. In modern accelerators an important fraction of the gas source is ascribed to particle induced desorption. In synchrotron radiation facilities, high-energy electron colliders and the LHC such a source of gas is the predominant one.

The **desorption yield** η , i.e. the number of molecules desorbed per impinging particle, is needed to design the vacuum system of particle accelerators.

$$\eta = \frac{\text{number of molecules desorbed}}{\text{number of particles impinging on the surface}}$$

η depends on many parameters, in particular on the nature of the particle, the material, and the gas. In addition, an important role is played by the quantity of particles that have already impinged on the surface, namely the dose D [particles/cm²]. The cleanliness of the surfaces has also a crucial influence.

4.3.1 Electron stimulated desorption (ESD)

For typical metals used in vacuum technology, the ESD yield of hydrogen is the highest followed by those for CO, CO₂ and CH₄, in decreasing order.

$$\eta_{H_2} > \eta_{CO} > \eta_{CO_2} > \eta_{CH_4}$$

For electron energy of about 300 eV and negligible dose, the order of magnitudes for η_{H_2} and η_{CH_4} are 10^{-2} and 10^{-4} molecules per impinging electron, respectively.

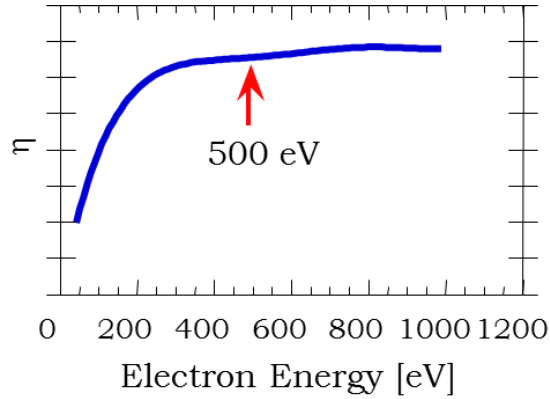


Fig. 27: ESD yield measured as a function of the electron energy. The values of η are arbitrary.

The ESD yields depend strongly on the impinging-electron energy up to 500 eV, while in the range 2-15 KeV they can be considered as constant. Most of the desorbed molecules are neutral; however, ions are also desorbed to a much lower extent (η is about 100 times lower). The desorbed molecules have average kinetic energy much higher than the thermal energy; in fact, they are ejected with energies of a few eV, up to 10 eV.

Electron bombardment cleans metallic surfaces by gas desorption. As a consequence, the desorption yields decrease when the electron dose increases. Except for water molecules, the measured η_e have a power law dependence on the dose of electrons D_e for doses higher than $10^{18} \text{ e}^- \text{ cm}^{-2}$:

$$\eta_e = \eta_0 D^{-\alpha} \quad (63)$$

where $0.6 < \alpha < 1$.

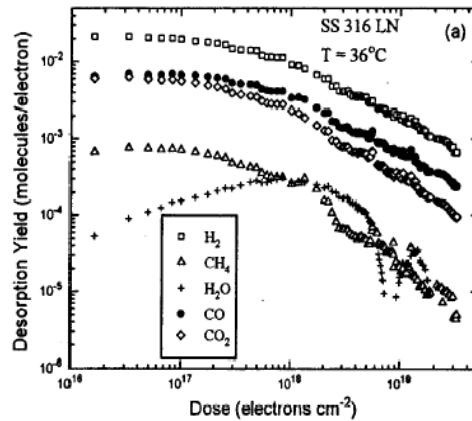


Fig. 28: Desorption yields measured for 316 LN stainless steel as a function of the electron dose. The sample was baked at 150°C for 24 h and 300 for 2 h [22].

The accumulated dose effect is lost when the surface is vented to air for long time. For short exposure to air (for example a few hours) a residual effect is measured; it is called ‘memory effect’: η values similar to those attained before venting are achieved after a smaller dose.

The total quantity of gas desorbed exceeds one monolayer. Some authors explain this result assuming a stimulated diffusion of C, O, and H atoms from the oxide layer of the materials.

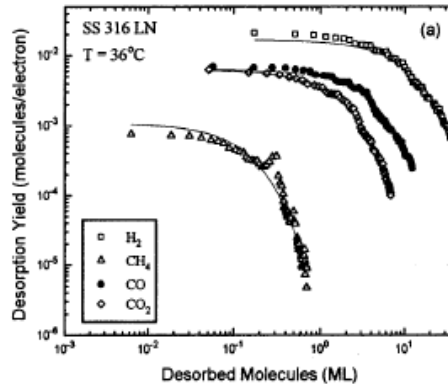


Fig. 29: Desorption yields measured for 316 LN stainless steel as a function of the quantity of desorbed molecules. One monolayer ML is equivalent to 2×10^{15} molecules cm^{-2} . The sample was baked at 150°C for 24 h and 300°C for 2 h [22].

4.3.1.1 The physical model of electron stimulated desorption

The ESD process can be considered as an isolated interaction between an electron and an adsorbate. The maximum energy ΔE transferred during the collision between a low energy electron of mass m_e and a molecule of mass M is calculated by classical kinematics. For hard-sphere scattering and $m_e \ll M$, one can estimate that [23]:

$$\frac{\Delta E}{E_e} \cong \frac{4m_e}{M} \quad (64)$$

For H_2 the fraction of energy transferred to the molecules is about $2/1840$. For typical electron energy of about 300 eV, ΔE is of the order of 0.1 eV. These values are much lower than the measured energies of desorbed molecules, typically in the 2-10 eV range. Therefore, the direct momentum transfer is not the dominant process in ESD. Electronic energy transfers are then considered.

One of the earliest ESD model was proposed by Menzel, Gomer, and Redhead (MGR model).

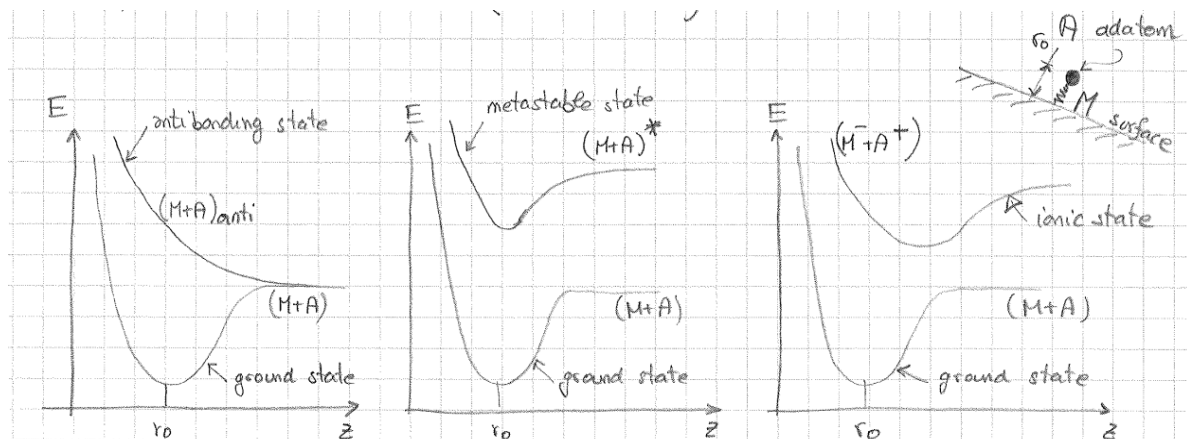


Fig. 30: Potential energy vs. distance diagram to illustrate the possible excited states of adatoms

The MGR model assumes that the metal-adsorbed molecule system is initially in its ground state: $(M+A)$ in Fig. 30. The interaction with the incident electron provokes an adiabatic transition (Franck-Condon principle) to excited states of different nature: antibonding $(M+A)^a$, metastable $(M+A)^*$, and ionic states (M^+A^+) . The adiabatic transition implies a change of electronic energy in about 10^{-16} s with a frozen distance z between nuclei. The transition is vertical in potential energy vs. distance diagram.

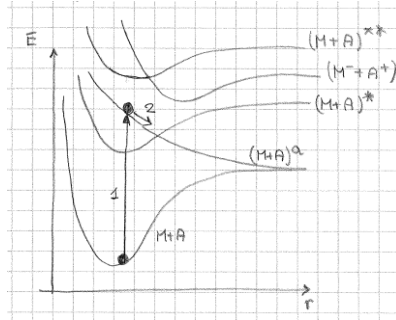


Fig. 31: Potential energy vs. distance diagram to illustrate the Frank-Condon transition to an antibonding state.

After the excitation, nuclear motion may occur over a time scale of about 10^{-13} - 10^{-14} s: part of the potential energy is converted into kinetic energy. The crossing of potential curves is possible (see fig 32) resulting in different de-excitation pathways.

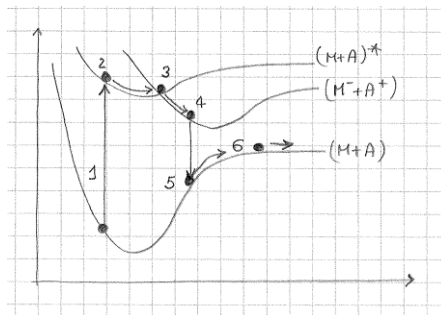


Fig. 32: Potential energy vs. distance diagram to illustrate the transition to different states and the final desorption of a neutral atom.

Whenever the original state is reached during the downward transition (rebonding), the molecule can escape if it has acquired enough kinetic energy to overpass the potential binding energy at the position of transition. The desorption as a stable neutral is possible when the downward transition occurs at a distance from the surface which is larger than a critical distance r_c .

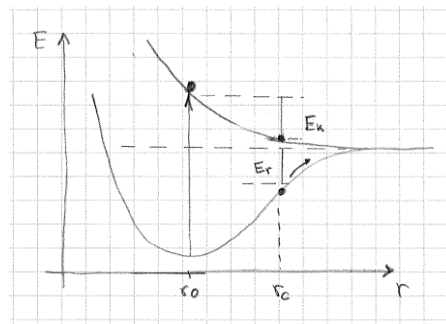


Fig. 33: Potential energy vs. distance diagram to illustrate the meaning of the critical distance r_c ; transition occurring at $r > r_c$ lead to the desorption of stable neutrals

For further details, see [24 and 25].

4.3.2 Photon stimulated desorption (PSD)

Particle beams emit photons whenever they are accelerated, namely whenever their velocity vectors are changed. Synchrotron radiation (SR) is emitted when charged particles moving with relativistic speeds are forced to follow curved trajectories in magnetic fields.

The emitted photons impinge on the wall of the vacuum system and may desorb gas molecules. There is experimental evidence that the photon stimulated desorption is generated by a two-step process:

1. The impinging photons extract photoelectrons.
2. The extraction and recapture of the photoelectrons stimulate the desorption of gas molecules by the ESD mechanism as shown in 4.3.1.

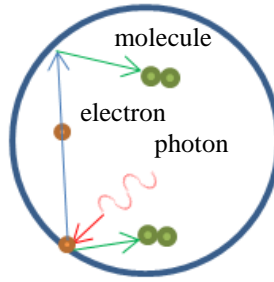


Fig. 34: Schematic picture showing the two steps of the photon stimulated desorption; the photon generate photoelectrons which are responsible for the gas desorption when leaving and reaching again the surface.

4.3.2.1 The spectrum of synchrotron radiation and its critical energy

A particle of charge 'e', energy E and rest mass m_0 , moving on a circular orbit (radius ρ) radiates electromagnetic radiation with the following power P_{rad} :

$$P_{rad} = \frac{e^2 c}{6\pi\epsilon_0 (m_0 c^2)^4} \frac{E^4}{\rho^2} \quad (65)$$

where ϵ_0 and c are the vacuum permittivity and the speed of light, respectively. Consequently, electrons emit much more synchrotron radiation power than protons for the same bending radius and energy:

$$\frac{(P_{rad})_{electrons}}{(P_{rad})_{protons}} = \left(\frac{m_p c^2}{m_e c^2} \right)^4 = 1.13 \times 10^{13} \quad (66)$$

The emitted power depends strongly on the beam energy and the radius of the bent trajectory. Synchrotron emission is strongly beamed along the direction of motion, which turns out to be perpendicular to the acceleration. The emission is concentrated into an angle of the order of $2/\gamma$ rad along the direction of motion (see Fig. 35), where γ is the Lorentz factor $\gamma = 1/\sqrt{1 - (v/c)^2} = E/mc^2$.

Synchrotron radiation from bending magnets has a very broad energy spectrum, which is characterised by the critical energy ϵ_c :

$$\varepsilon_c = \frac{3}{2} \frac{\hbar c}{\rho} \gamma^3 = \frac{3\hbar c}{2(mc^2)^3} \frac{E^3}{\rho} \quad (67)$$

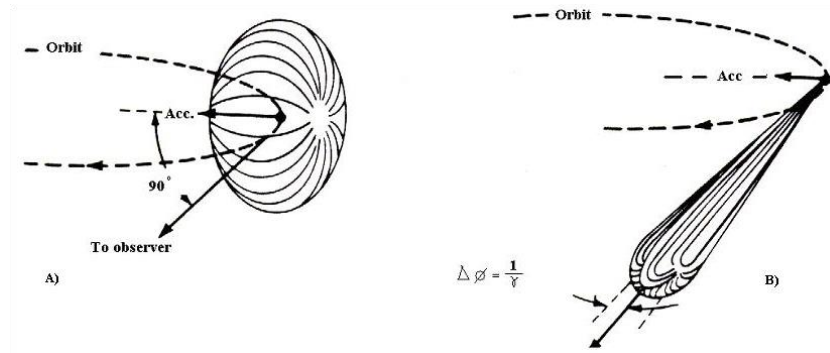


Fig 35: Emission of synchrotron light from non-relativistic (A) and relativistic (B) charged particles. Courtesy of Wikipedia.

The critical energy subdivides the photon spectrum in two parts of equal emitted power. In practical units, for electrons:

$$\varepsilon_c [\text{KeV}] = 0.665 \times E^2 [\text{GeV}^2] \times B [\text{T}] \quad (68)$$

and for protons:

$$\varepsilon_c [\text{KeV}] = 1.1 \times 10^{-10} \times E^2 [\text{GeV}^2] \times B [\text{T}] \quad (69)$$

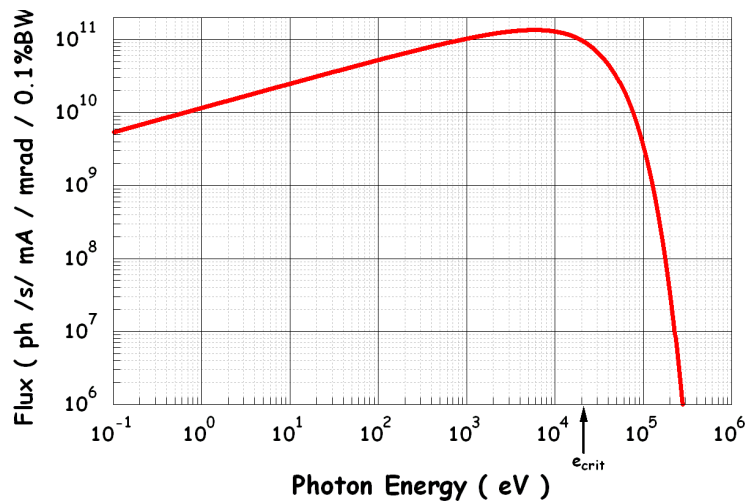


Fig. 36: Emitted photon spectrum for the ESRF: $E=6\text{GeV}$, $\varepsilon_c=20504\text{ eV}$, bending radius= 23.366 m

It can be shown that the number of emitted photon per unit time:

$$\dot{N} = \frac{15\sqrt{3}}{8} \frac{P_{rad}}{\varepsilon_c} \quad (70)$$

and the mean photon energy is:

$$\dot{N} = \frac{P_{rad}}{\langle \varepsilon \rangle} \rightarrow \langle \varepsilon \rangle = \frac{8}{15\sqrt{3}} \varepsilon_c \quad (71)$$

In practical unit

$$\dot{N} = 8.08 \times 10^{17} I [mA] E [GeV] \quad (72)$$

The linear flux, i.e. the emitted photons per second and meter, is given by:

$$\frac{d\dot{N}}{ds} = 1.28 \times 10^{17} \frac{I [mA] E [GeV]}{\rho [m]} \quad (73)$$

4.3.2.2 The photon desorption yield η_{ph}

The average number of molecules desorbed per impinging photon, namely the photon desorption yield, has been measured with synchrotron radiation of different critical energy. The η_{ph} values are in general plotted as a function of the dose of impinging photons per unit length of vacuum chamber.

η_{ph} does not depend significantly on the photon dose D up to about 10^{20} photons/m. For higher doses, η_{ph} varies as a power law function of the dose:

$$\eta_{ph} \propto D^{-\alpha} \quad (74)$$

The values of α are in the range 0.6 to 1, as for electron stimulated desorption.

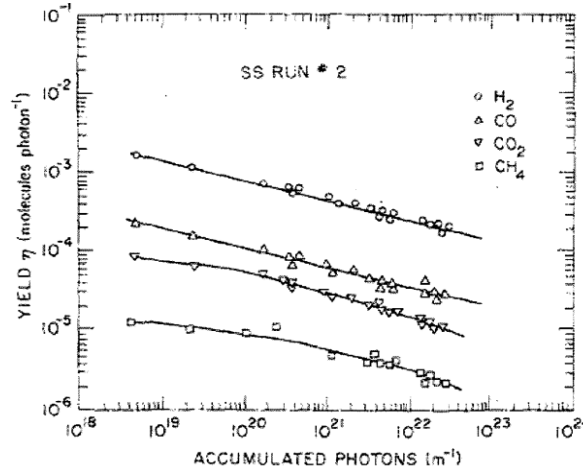


Fig. 37: Photon desorption yields for baked stainless steel as a function of the accumulated dose of photons [26]

Photons with energy lower than the photoelectron extraction threshold (workfunction, about 5 eV for metals used in UHV) do not stimulate gas desorption. η_{ph} depends linearly on the critical energy of the photon spectrum when $\varepsilon_c < 280$ eV:

$$\eta_{ph} \propto \varepsilon_c^\beta \quad (75)$$

where $0.74 < \beta < 1.12$.

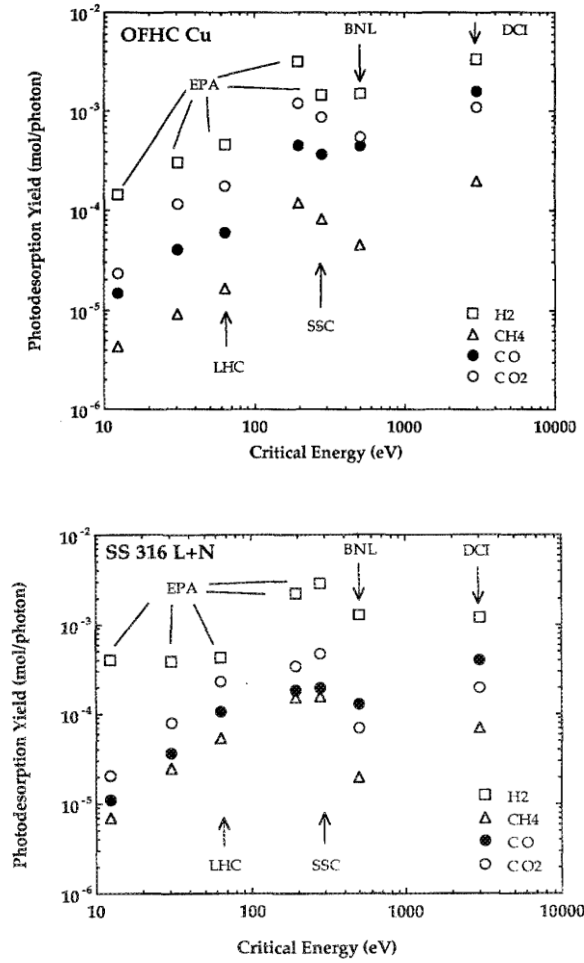


Fig. 38: Photon desorption yield as a function of the critical energy for 316LN stainless steel and copper [27]

For critical energy in the range 0.5-1 KeV, the order of magnitude of η_{ph} for the four most desorbed molecules is shown in Tab 17.

Table 17: Orders of magnitude of photon desorption yield for critical energies in the range 0.5-1 KeV. Cleaned and in situ baked Cu or stainless steel. No photon dose effect.

| Gas | η |
|-----------------|---|
| | $\left[\frac{\text{molecules}}{\text{photon}} \right]$ |
| H ₂ | 10^{-3} |
| CO | 10^{-3} - 10^{-4} |
| CO ₂ | 10^{-3} - 10^{-4} |
| CH ₄ | 10^{-5} |

4.3.3 Methods for the reduction of electron and photon stimulated desorption.

The gas desorbed by electrons or photons is extracted from the surface of vacuum chambers or from the first tenths of atomic layers underneath. Therefore, a state of art **surface cleaning** is essential to avoid excessive desorption. A beneficial effect is obtained by **in situ bakeout** at temperature higher than 120°C; heating the material results in a cleaner surface; however, the effect on the η values is limited and, in general, less than a factor of 10.

In the example of Fig. 39, after bakeout at 150°C, the η values for copper of H₂, CO, CO₂, and CH₄ are reduced by a factor in the range 1.5 to 2.5. The reduction is more pronounced for H₂O (about 35 times lower) [27].

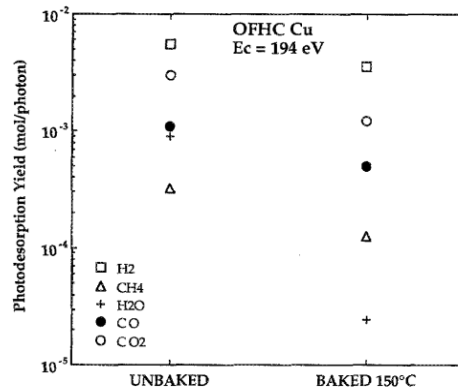


Fig. 39. Photon desorption yields of baked and unbaked copper. The critical energy is 194 eV [27].

Electropolishing and vacuum firing have a very limited effect on the η values. Air exposure after these treatments oxidizes again the surface and regenerates the gas source.

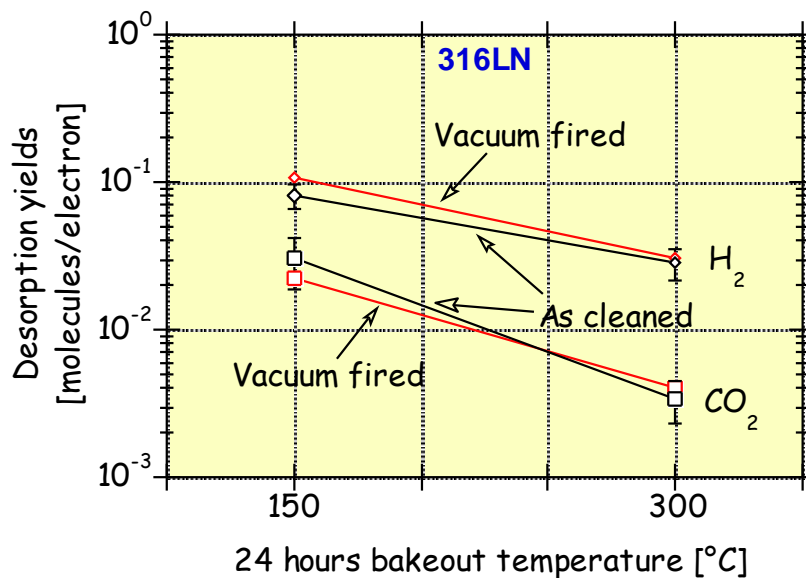


Fig 40: Electron desorption yields for 316LN stainless steel after bakeout. The effect of vacuum firing is shown for H₂ and CO. The same effect was measured for CH₄ and CO₂.

As shown in 4.3.1 and 4.3.2, the accumulated dose effect lead to a significant reduction of the desorption yields. Power law reductions are measured for both accumulated electron and photon impingements.

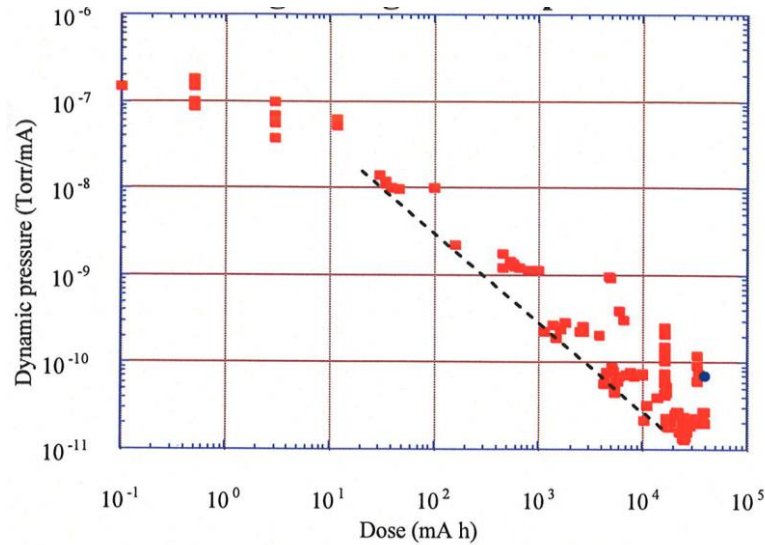


Fig. 41: Reduction of the pressure variation induced by photon desorption yield in the first operational period of the Large Electron Positron collider [28]. The beam dose (mA h) is proportional to the number of photons that hit the vacuum chambers.

Particle accelerators, whose performance is limited by beam induced desorption, are run at progressively increasing current to accumulate photon or electron dose on the vacuum chambers and consequently reduce the desorption yields. This operation is called ‘**beam conditioning**’ or ‘**beam scrubbing**’ of the vacuum chambers. It can last several hours to several days.

Another radical method to reduce stimulated desorption is coating the inner wall of the beam pipes with a thin non-evaporable getter film. After in situ bakeout at temperature higher than 180°C, the oxide layer covering the film is dissolved leaving an extremely clean surface. These materials are considered in the chapter dedicated to pumps.

4.3.4 Ion stimulated desorption (ISD)

Ion induced desorption is relevant in two different conditions.

1. Beam particles may collide with the residual gas and create ions (H_2^+ , CH_4^+ , CO^+ , CO_2^+ , etc.). If the beam is made of positively charged particles, the ions are accelerated by the beam potential and collide on the nearby walls with energy between 1 eV to several KeV. The collision results in gas desorption. Desorption yield are measured in dedicated laboratory set-ups.
2. When heavy ions are accelerated, beam losses may lead to collision of high-energy heavy ions with the wall of the vacuum system. Typical ions are Pb^{53+} , U^{73+} , and Ar^{10+} . Experimental studies have been carried out with beam energy in the range from 1 MeV/nucleon to 100 GeV/nucleon. In this case, the desorption yields may be orders of magnitude higher than those for residual-gas ions.

4.3.4.1 Desorption stimulated by residual-gas ions

The desorption mechanism induced by residual-gas ion collision can be depicted as the effect of a series of collisions among the impinging ion, the atoms of the metal and the adsorbed molecules [28]. The desorption yields η_i depends on the ion mass and energy, the nature of the desorbed

molecule, and the material of the vacuum chamber [29]. Ions are more effective in desorbing gas than electrons and photons. Typical η_i values for baked copper and ion energy of about 1 KeV are about 1 for H_2 and CO ; 5 and 10 times lower for CO_2 and CH_4 , respectively.

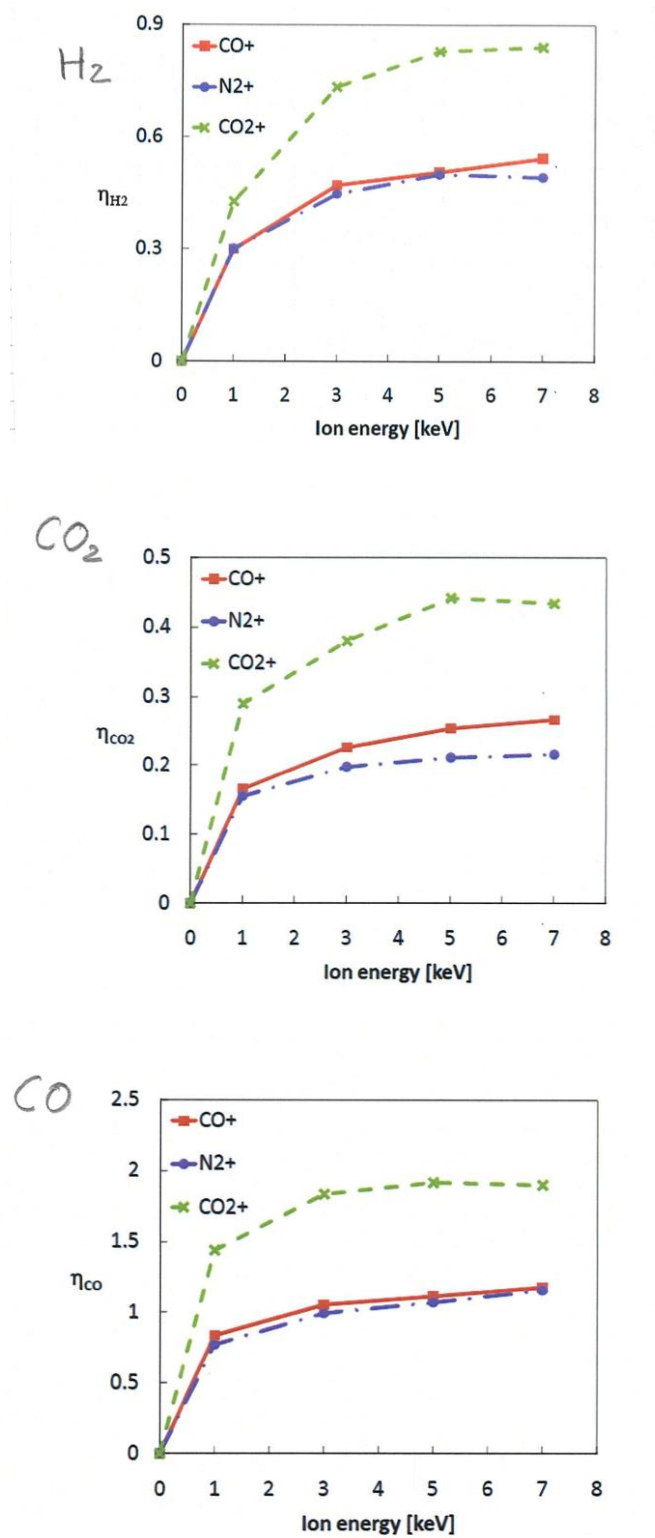


Fig. 42: H_2 , CO_2 and CO desorption yields of N_2^+ , CO^+ and CO_2^+ ions incident on copper as a function of ion energy [29]

The reduction of the η_i with increasing ion dose has been measured for more than 10^{15} ions/cm². However, there are indications that the reduction is limited to a factor of 10 for doses higher than 10^{16} ions/cm².

Ion induced desorption has been described in terms of ion energy loss:

$$\frac{dE}{dx} = N \cdot S(E) \quad (76)$$

where: N is the number of atoms in the solid; S(E) is the stopping power cross section which depends on the energy E of the impinging ions.

S(E) takes into account two different phenomena. The first is called the nuclear stopping power $S_n(E)$; it considers the energy transferred to the nuclei of the material through multiple scattering and change of the trajectories. This energy transfer mechanism is dominant up to about 50 KeV ion energy and dominate the desorption induced by residual-gas ions.

The second energy transfer mechanism is called the electronic stopping power $S_e(E)$ which models the interactions with the electrons of the material, firstly to break the bonding with the nuclei and then to accelerate them. The transfer of energy to electrons provokes a thermal spike that finally cause the gas desorption. This process prevails at energies higher than 1 MeV.

4.3.4.2 Desorption stimulated by high-energy heavy ions

In the last 15 years, several experiments have shown that high energy ($E > 1$ MeV/nucleon) ions can induce the desorption of a huge quantity of gas molecules. Desorption yield up to 10^5 molecules/ion were measured for In^{49+} at 158 GeV/nucleon at the CERN SPS. A review of data is available in ref. [30]. The beneficial effect of the accumulated dose is still valid for heavy ion [30].

It has been shown that the desorption yields are correlated with the electronic energy loss by means of a power law:

$$\eta_i \propto \left(\frac{dE}{dx} \right)_e^n \quad (77)$$

with $2 < n < 3$.

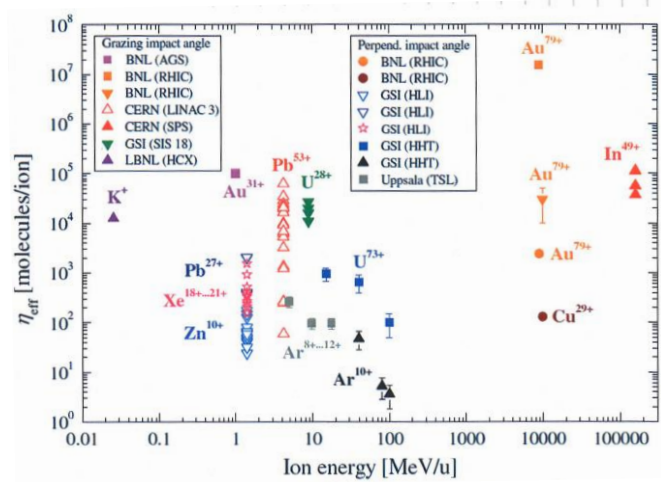
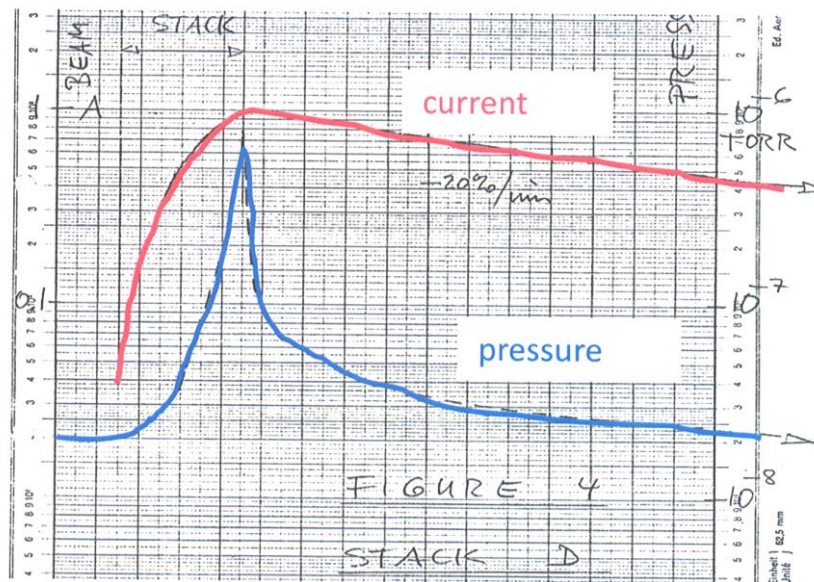


Fig. 43: Heavy-ion desorption yield (all molecules included) [30]

4.3.5 Pressure runaway provoked by ion stimulated desorption

Ion induced desorption can trigger a rapid pressure rise in accelerators where positive beams circulate. The pressure instability is then the cause of a lower beam lifetime and, if the pressure interlocks are attained, even to beam dump. This phenomenon was shown first at the CERN ISR when increasing the proton current to about 1 A (see Fig. 44).

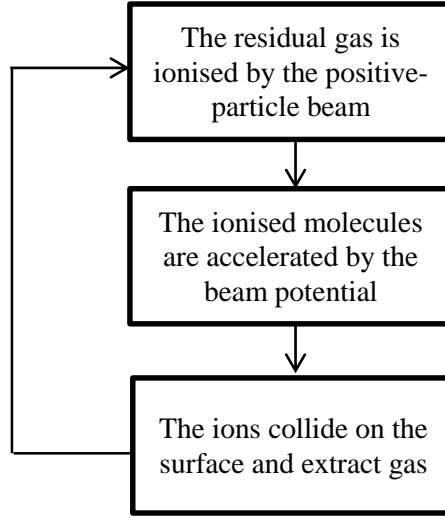


First documented pressure bump in the ISR

E. Fischer/O. Gröbner/E. Jones 18/11/1970

Fig. 44: Pressure and beam current evolution in the ISR [31]. The pressure bump starts when the current attains a critical value.

The pressure rise is generated by a positive feedback process that can be depicted with the following block diagram.



The critical current at which the runaway process starts can be obtained in the following way.

1. The total gas flow of desorbed molecules per unit length of vacuum chamber is:

$$Q = \eta_i \cdot \sigma_i \frac{PI}{e} + Q_{th} \quad (78)$$

σ_i is the cross section of ionisation of the gas molecules; I the beam current; P the pressure; Q_{th} the thermal outgassing which does not depend on the beam current. The ionisation probability for one proton is $\sigma_i n = \sigma_i P / k_B T$ and the flow of circulating protons is I/e .

2. The pressure in the beam pipe is:

$$P = \frac{Q}{S_{eff}} = \eta_i \sigma_i \frac{PI}{S_{eff} e} + \frac{Q_{th}}{S_{eff}} \rightarrow P = \frac{Q_{th}}{S_{eff} - \eta_i \sigma_i \frac{I}{e}}$$

3. The pressure diverges when:

$$S_{eff} - \eta_i \sigma_i \frac{I}{e} \rightarrow 0$$

from which an expression for the critical current can be obtained:

$$I_c = \frac{S_{eff} e}{\eta_i \sigma_i} \quad (79)$$

For an effective pumping speed of 10 l s^{-1} and an ionisation cross section of 10^{-18} cm^2 (CO ionised by protons at 26 GeV, see Tab. 18), the critical current is about 16 mA if the desorption yield is 1.

Table 18: Values of the ionisation cross section at two different proton-beam energies [32]

| Gas | σ_i [10^{-18} cm2] | |
|-----------------|--|--------------|
| | 26 GeV | 7 TeV |
| H ₂ | 0.22 | 0.37 |
| He | 0.23 | 0.38 |
| CH ₄ | 1.2 | 2.1 |
| CO | 1.0 | 1.8 |
| CO ₂ | 1.1 | 2.0 |
| Ar | 1.6 | 2.8 |

5 Gas pumping

Vacuum pumps in molecular regime are classified in two families: momentum transfer pumps and capture pumps; both act on each molecule singularly since no momentum and energy transfer is possible between molecules in this pressure range. In the first family, molecules receive a momentum component pointing towards the pump outlet (foreline) where the gas is compressed and evacuated by pumps working in the viscous regime (for example: rotary vane, diaphragm, and scroll pumps). The second family removes gas molecules by fixing them on a surface exposed to the vacuum.

5.1 Momentum transfer pumps

In this family of pumps, gas molecules are steered by collision with moving surfaces (molecular pumps) or supersonic jets (diffusion pumps). The latter mechanism is not anymore used in particle accelerators, though it still has extensive applications in industrial vacuum.

5.1.1 Molecular pumps

In molecular pumps, gas molecules impinge and adsorb on the moving surface; on desorption, the molecular emission is not anymore isotropic due to the superposition of the wall velocity (see Fig.45). As a result, molecules are preferentially redirected towards the direction of the wall movement, i.e. the density of molecules increases in the same direction.

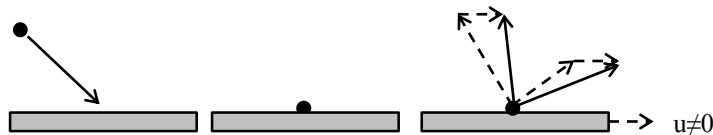


Fig. 45: Schematic drawing showing the mechanism of momentum transfer by collision onto a moving surface

The first molecular pump was invented by W. Gaede. In the original design, the moving surface is a rotor revolving at high frequency (see Fig. 46).

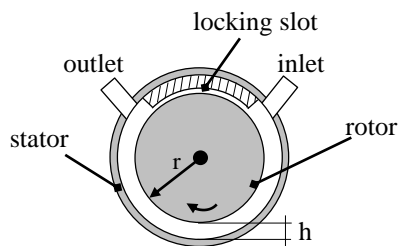


Fig. 46: Schematic drawing of a molecular pump.

To prevent backstreaming, the inlet and the outlet were separated by a very thin slot (locking slot). The slot height was of the order of 10^{-2} mm.

The most important characteristics of a molecular pump are the pumping speed S and the maximum compression pressure ratio that can be achieved between the pump inlet P_{IN} and outlet P_{OUT} :

$$K_0 = \left(\frac{P_{OUT}}{P_{IN}} \right)_{MAX} \quad (80)$$

The crucial parameters affecting S and K_0 are highlighted by a simplified model (see Fig. 47).

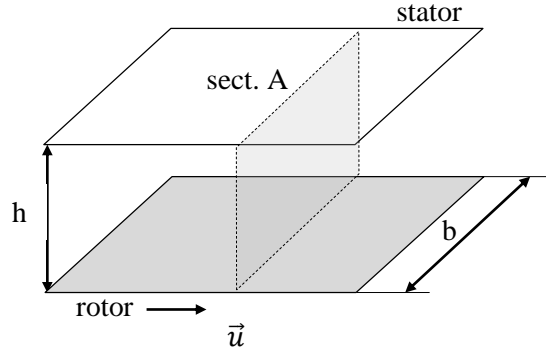


Fig. 47: Plane section of a molecular pump

At any time, half of the molecules have just collided with the moving surface (rotor) and drift in the direction of the velocity \vec{u} . The other half hits the stator where the drift component is lost. As a result, the drifted molecular flow Q_p towards an imaginary section A (see Fig. 47) is:

$$Q_p = \frac{1}{2} n \cdot u \cdot b \cdot h = \frac{1}{2} \frac{P}{k_B T} \cdot u \cdot b \cdot h$$

Where ‘bh’ is the area of the cross section A and ‘ubh’ is the gas volume drifting through section A in one second. Converting in pressure-volume units and dividing by P, the pumping speed is obtained:

$$S = \frac{Q_p}{P} = \frac{1}{2} u \cdot bh \quad (81)$$

Therefore, the pumping speed of molecular pumps is proportional to the speed of the moving wall. It does not depend on the nature of the gas; thus, molecular pumps are not selective. Finally, a large cross section ‘bh’ is needed to receive a large quantity of gas.

The moving wall produces a higher gas density near the pump outlet. In turn, the pressure gradient generates a gas backflow Q_{bf} that can be written as:

$$Q_{bf} = -\bar{c} \nabla P$$

where \bar{c} is the conductance of the unit-length duct of cross section area bh. For $h \ll b$:

$$\bar{c} = \frac{2}{3} \frac{(bh)^2}{b+h} \langle v \rangle$$

The net flow is therefore given by:

$$Q = Q_p - Q_{bf} = \frac{1}{2} P u bh - \bar{c} \nabla P$$

When the net flux is zero, the maximum compression ratio is reached; in this case:

$$\frac{dP}{P} = \frac{1}{2} \frac{u bh}{\bar{c}} dx$$

Integrating between inlet and outlet (distance L) and using Eq. 13 and 20:

$$K_0 = \left(\frac{P_{OUT}}{P_{IN}} \right)_{MAX} = \exp\left(\frac{u bh L}{\bar{c}}\right) \propto \exp\left(\frac{u}{\langle v \rangle} \frac{L}{h}\right) \propto \exp\left(u \sqrt{m_i} \frac{L}{h}\right) \quad (82)$$

To obtain high K_0 :

- the velocity of the moving surface must be of the order of the mean molecular speed (high $\frac{u}{\langle v \rangle}$ ratio),
- the duct where molecules drift must be narrow and long (high $\frac{L}{h}$),

In addition, K_0 depends strongly on the molecular mass, the lowest being for H_2 . As a result, the ultimate pressure of molecular pumps is dominated by H_2 . More generally, the low K_0 for H_2 is an intrinsic limitation of momentum transfer pumps.

5.1.2 Turbomolecular pumps

For many years, the industrialisation of molecular pumps was hindered by the machining of the locking slot. The narrow gap between rotor and stator created mechanical issues due to tolerances and thermal expansion. The problem was overcome in 1957 when W. Becker invented the turbomolecular pump (TMP). In the TMP, the momentum transfer is produced by rapidly rotating blades rather than parallel surfaces.

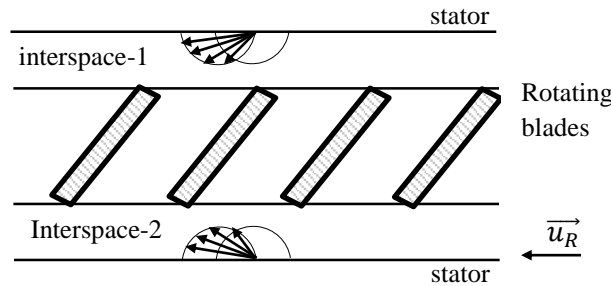


Fig. 48: A single rotor-stator stage in a turbomolecular pump. The molecular speed distributions are drawn as seen from the rotating blade. \vec{u}_R is the stator speed seen by the rotating blades.

The rotating blades are tilted with respect to the rotational axis. As a result, oblique channels between successive blades are formed. The rotor is inserted between two static surfaces defining two interspaces (see Fig. 48). When the molecule comes from interspace-1, the angular distribution of the molecular velocity seen from the blades is preferentially oriented towards the blades' channels. Conversely, for those coming from interspace-2, the velocity vectors point preferentially towards the blades' wall, therefore increasing backscattering. A gas flow is consequently generated from interspace-1 to interspace-2. This mechanism works only if the angular distribution of the molecular speed as seen from the blade is significantly deformed, i.e. only if the blades' speed is at least of the order of the mean molecular speeds (hundredths of $m s^{-1}$).

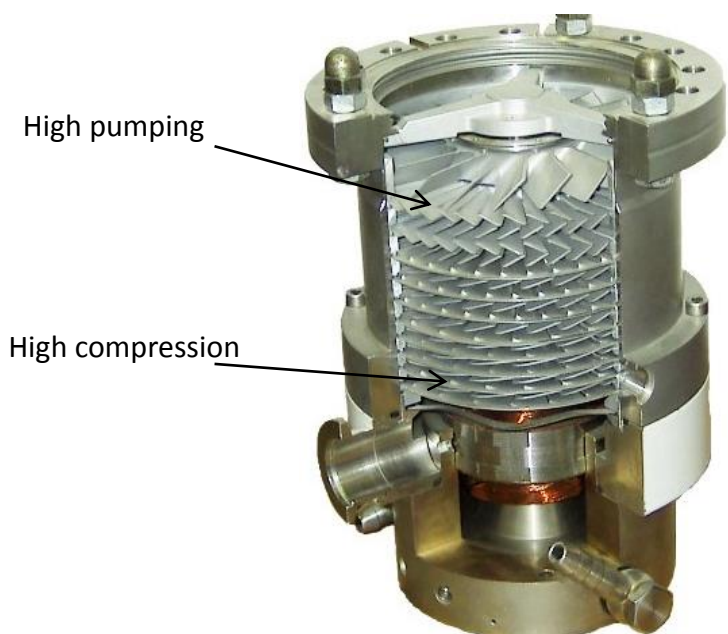


Fig. 49: Cut view of a turbomolecular pump. Courtesy of Wikipedia
(http://en.wikipedia.org/wiki/Turbomolecular_pump)

In the real turbomolecular pump, the gas is compressed by several series of rotating blades (see Fig. 49). Every series of rotating blades is followed by a series of static blades. Molecules transmitted through the rotating blades' channels hit the static blades; as a result, the angular distribution of velocity is randomized and the molecules are ready for the next compression stage. The momentum transfer is effective only if the molecules do not experience inter-molecular collisions after hitting the blades; this is equivalent to say that the mean free path has to be larger than the blade distances. As a result, this type of pumps works at full pumping speed only in molecular regimes ($P < 10^{-3}$ mbar).

The conclusions drawn for molecular pumps hold also for turbomolecular pumps. The dimension of the blades and the distance rotor-stator are larger for the first series of blades in view of maximising the pumping speed (see Eq. 81). The last compression stages are tighter to increase the maximum compression ratio (see Eq. 82) and compensate for the increased gas density and thus for the resulting lower molecular mean free path. The pumping speed of TMP is constant in molecular regime ($P < 10^{-3}$ mbar) and ranges between 10 and 3000 $\ell \text{ s}^{-1}$ depending on pump inlet diameter, and mechanical design. As expected, the maximum compression ratio is the lowest for H_2 ; in classical designs it is about 10^3 (see Fig. 51). Nowadays values up to 10^6 are achieved by integrating a molecular drag pump (Gaede or Holweck drag stage) to the rear of the blade sets.

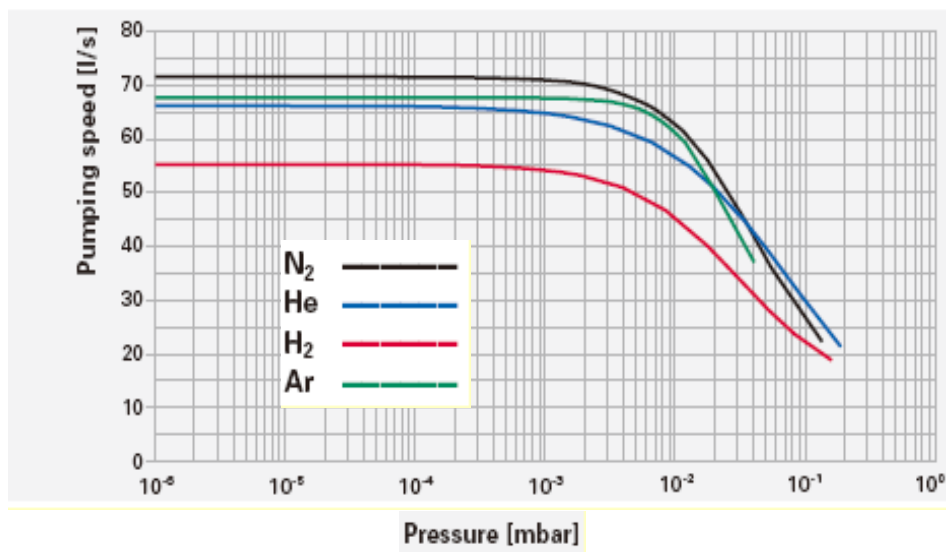


Fig. 50: Pumping speeds of a turbomolecular pump equipped with a DN63CF flange. For TMP, the pumping speeds are constant in the free molecular regime and the nature of the pumped gas has a limited effect, if compared with other type of pumps. Courtesy of Pfeiffer Vacuum.

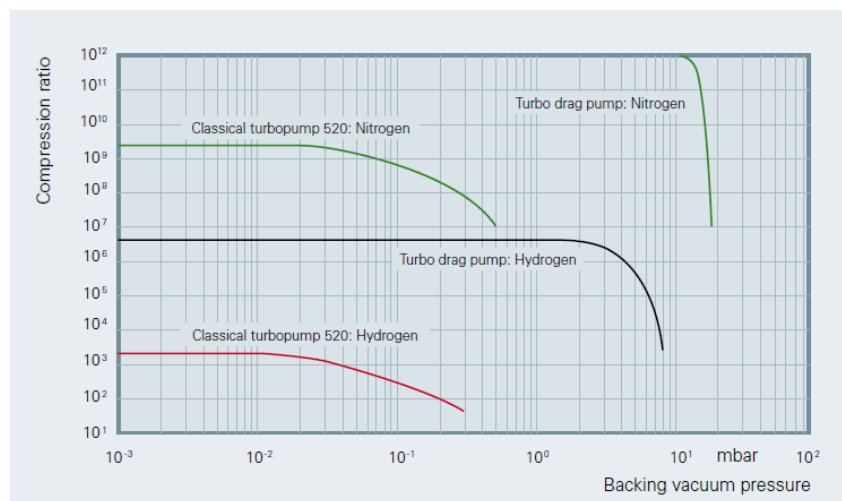


Fig. 51: Maximum compression ratio of two different turbomolecular pumps for N₂ and H₂. Courtesy of Pfeiffer Vacuum

The TMP ultimate pressure is of the order of 10^{-10} - 10^{-11} mbar for baked and all-metal vacuum systems. Lower pressures may be obtained if another type of pump removes the TMP H₂ backstreaming.

At the pump outlet, the compressed gas is evacuated by a mechanical pump (often called backing pump) operating in viscous regime. The turbomolecular and its backing pump are in general assembled in a single unit that includes power supplies, controls and instrumentation.

Each set of rotor blades is machined from a single block of high-strength aluminium alloys. Typical pumps equipped with a DN 100 flange rotate at a frequency of 1 KHz, therefore approaching circumferential speeds up to 500 m s^{-1} .

The TMP is the best available pump for the first stages of ion sources. It can evacuate high gas flow at relatively high pressure without selectivity and memory effects. For example, a DN100 TMP can withstand a continuous gas flow up to $2 \cdot 10^{-1}$ mbar $l \text{ s}^{-1}$ without damage.

The use of dry pumps for TMP backing has surmounted the risk of oil backstreaming from rotary vane pumps. The higher ultimate pressure of dry pumps is compensated by the integration of molecular drag pumps (higher compression ratio). The complete removal of all lubricated mechanical bearing has been obtained by magnetic rotor suspension.

The main drawback of TMP is related to possible mechanical failures leading to definitive damage of the high-speed rotor. In addition, in case of unwanted rotor deceleration caused by power-cut or rotor seizing, the vacuum system has to be protected by safety valves and dedicated pressure sensors against air backstream. TMP have limited application in radioactive environment due to possible damage to the embarked electronics and power supplies. Some radiation resistant TMP are nowadays available; with a significant cost, the whole electronics is moved beyond the radiation shielding by means of long cables.

5.2 Capture pumps

Capture pumps remove gas molecules by fixing them onto an internal wall. To be efficient, capture pumps must block the gas molecules for an average time (sojourn time t_s) much longer than the typical running time of the accelerator. An estimation of the sojourn time is given by the Frenkel law [33].

$$t_s = t_0 e^{\frac{E_a}{k_B T}} \quad (83)$$

where E_a is the adsorption energy and $t_0 \approx \frac{h}{k_B T} \approx 10^{-13}$ s. Very long sojourn times are obtained either for high adsorption energies :

$$E_a \gg k_B T$$

or for very low temperatures :

$$T \ll \frac{E_a}{k_B}$$

In the former case, capture pumps are called ‘chemical pumps’ or ‘**getter pumps**’; in the latter, ‘**cryogenic pumps**’.

In chemical pumps, the binding force involves electron exchange between gas molecules and surfaces (**chemisorption**). Typical binding energies for getter pumps are higher than 1 eV/molecule. In cryogenic pumps, Van der Waals interactions might be sufficiently strong to fix molecules to cold surfaces (**physisorption**). In this case, the binding energy can be much lower than 0.5 eV/molecule.

Chemisorption, implantation and physical burial of gas molecules by reactive metal atoms are combined in sputter ion pumps. They represent the most important and widely used pumping technology in particle accelerators.

5.2.1 Sputter ion pumps

In Sputter Ion Pumps (SIP) the residual gas is ionized in a Penning cell (see Fig. 52). The ions are then accelerated towards a cathode made of a reactive metal. The cathode-ion collisions provoke sputtering of reactive-metal atoms that are deposited on the nearby surfaces. The Penning cells are assembled in honeycomb structures to form the pump’s elements.

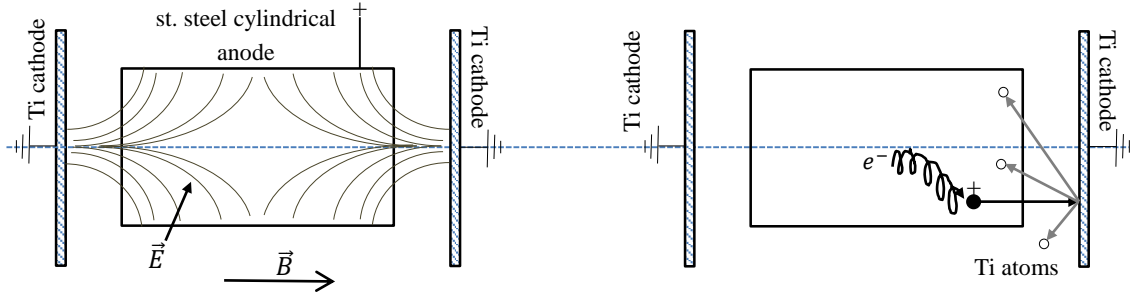


Fig. 52: Schematic drawing depicting the pumping mechanism of sputter ion pumps in the diode configuration

The pumping action is given by three distinct mechanisms:

- Chemical adsorption of gas molecules onto the reactive metal layer and subsequent burial by additional sputtered atoms; it works for all gas species except for rare gases, which cannot form chemical compounds.
- Implantation of both gas ions in the cathode and of energetic neutrals bounced back from the cathode into the deposited film; this is the only pumping mechanism for rare gas.
- Diffusion into the cathode material and the deposited film; this is possible only for H_2 because of its very large diffusivity in metals in its atomic form.

In the diode SIP (see Fig. 52), the anode is composed of several open cylinders made of stainless steel at a positive electrical potential (from 3 to 7 kV). The cathodes are plates of Ti -at ground potential- placed a few millimetres from both anode extremities. A magnetic field parallel to the cells' axis is generated by external permanent magnets (about 0.1 T). In this configuration, the crossed electrical and magnetic fields trap electrons in long helical trajectories resulting in an increased probability of gas ionisation.

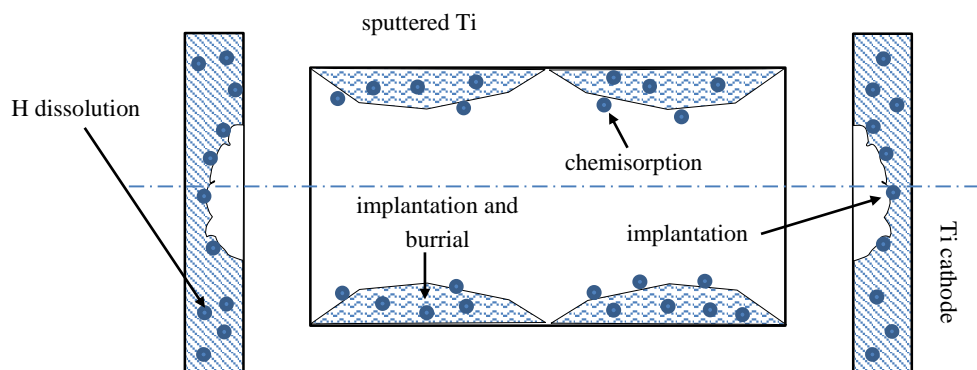


Fig. 53: Schematic drawing of a SIP cell after prolonged operation

Molecular implantation in the cathodes is not a permanent pumping; in fact, the progressive erosion due to gas ion sputtering soon or later frees the implanted gas. Once released from the cathodes, reactive gas species are chemisorbed while rare gases remain in the gas phase until the next implantation. Pressure instabilities have been reported after excessive pumping of rare gas: the continuous erosion liberates gas that increases the pressure, which in turn increases the erosion. Consequently, a pressure rise is generated; this is stopped when most of the rare gas is implanted in a deeper zone of the cathode. A new pressure spike appears when the erosion reaches the new rare gas front. This type of instability is typically observed when large quantities of air are pumped (Ar 1% in air) and are known as ‘argon disease’ [34].

The pumping efficiency for rare gas is improved by reducing the number of ions implanted into the cathodes, while increasing the energetic neutrals bounced back from the cathode and their chance to be buried by Ti atoms onto the anode. Two different approaches have been commercially exploited:

- cathodes made of higher atomic mass metals;
- different geometry than the diode configuration.

In the first case, Ta is used instead of Ti (181 amu against 48 amu). Gas ions, once neutralised on the cathode surface, have a higher probability to escape from the cathode and bounce back with higher energy when colliding on Ta than Ti. Consequently, the implantation probability on the anode is higher and the quantity of gas implanted into the cathode is lower. The pump that use Ta cathodes are called ‘noble diode’ or ‘differential ion pumps’.

In the second one, the diode configuration is modified by introducing a third electrode (triode sputter ion pumps, see Fig. 54). The cathode consists of a series of small Ti plates aligned along the cell axis and polarized negatively with respect to the ground. The anode is at the ground potential.

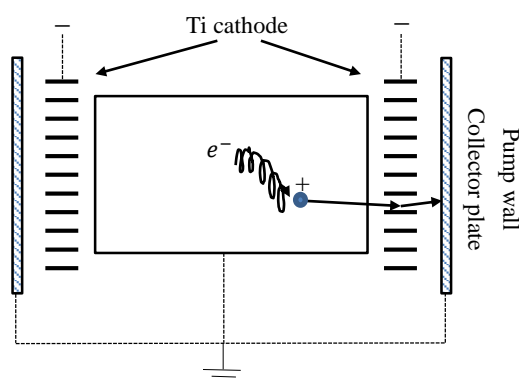


Fig. 54: Schematic drawing of the a triode SIP cell. The Ti cathodes are negatively biased

In this configuration, the collisions between ions and cathode are at glancing angle: the sputtering rate, the neutralisation and the bouncing probability are higher. As a result, more Ti atoms are sputtered and more gas molecules are implanted into the collector plate and anode; the gas implanted into the cathode is minimized.

An improved triode pump is the StarCell® produced by Agilent. Two sheets of Ti that are cut and bent to form radial blades (see Fig 55) replace the series of small plates. This increases the rigidity of the cathode and reduces the risks of short circuits.

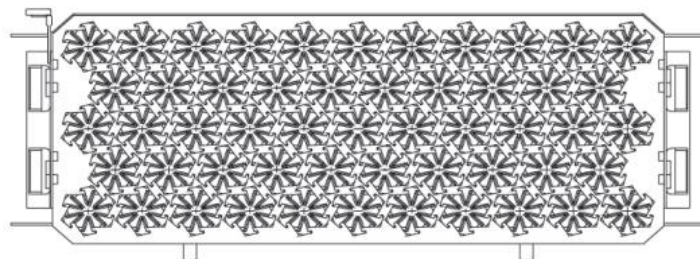


Fig. 55: Drawing of the Agilent's Star Cell Ti cathode. Courtesy of Agilent Vacuum.

5.2.1.1 Hydrogen pumping by SIP

In SIP, H_2 is mainly pumped by dissolution into the Ti cathodes. To be absorbed, H_2 must be dissociated. Because in the Penning discharge only a small fraction of the hydrogen ions are H^+ , the dissociation is possible only on the Ti cathodes after removal of the oxide layer by sputtering. This surface cleaning process is very slow if H_2 is the leading gas in the vacuum system due to its low sputtering yield (0.01 at 7 KeV on Ti). Therefore, at the beginning of the operation the pumping speed for H_2 is lower than the nominal and increases gradually with time.

The simultaneous pumping of another gas has a strong effect on H_2 pumping efficiency. If the additional gas has a higher sputtering yield, the cathode cleaning is faster and the nominal pumping speed is reached in a shorter time. Conversely, it can contaminate the cathode surface and reduce the H_2 adsorption. Finally, dissolved H atoms can be sputtered away reducing the pumping efficiency.

When the concentration of H_2 in the cathodes is higher than the solubility limit in Ti, hydride precipitates are formed. The cathodes expand and become brittle generating anomalous field emission and short circuit. A typical concentration limit is 10000 mbar l for commercial 500 ℓ s^{-1} SIP. Water vapour pumping also contributes to the total quantity of H_2 charged in the cathodes.

During the pumping of H_2 or after the dissolution of high quantity of the same gas, the operation of SIP at high pressures (higher than 10^{-5} mbar) can lead to thermal run-away. The Penning discharge heats the cathode and provokes gas desorption, which reinforces the discharge. This positive feedback mechanism can cause a local melt of the cathode. To avoid this problem, the electrical power provided to the pump is limited at high pressure and during the ignition.

5.2.1.2 Pressure measurement by SIP

The ion current collected by the SIP's cathodes is used as an indication of the pressure. In fact, a defined relationship is measured between the two variables down to pressures of the order of 10^{-9} mbar. For lower pressures, the pump current is limited by field emission (leakage current). The low-pressure reading can be extended by one decade if the applied voltage is reduced in the lower pressure range (for example from 7 to 3 kV). The pressure reading by SIP is extensively used in particle accelerators.

5.2.1.2 Pumping speed of SIP

The pumping speed of SIP depends on the gas pressure at the pump inlet, the nature of the gas, and the quantity of gas already pumped. The latter dependence is correlated with the implantation into the cathode. For new pumps and gases other than H_2 , the rate of implantation is larger than the rate of release by sputtering. Conversely, for 'saturated' pumps, the two rates equate and the pumping in the cathode is negligible. The nominal pumping speed of SIP is in general given for 'saturated' pumps.

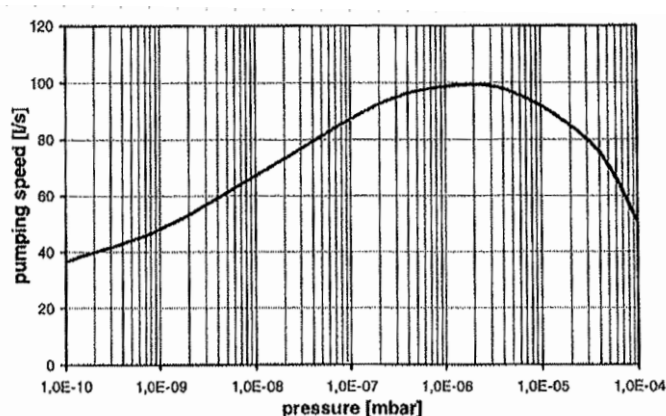


Fig. 56: Typical inlet-pressure dependence of SIP pumping speed; maximum pumping speed is reached at about 10^{-6} mbar. Courtesy of Agilent Vacuum.

The pumping speed attains a maximum for inlet pressures of about 10^{-6} mbar. This is the value given by the suppliers for the nominal pumping speed. For lower pressures, the pumping speed decreases, half of the maximum is obtained at about 10^{-9} mbar (see Fig 56). Typical values of S are collected in Tab. 19 and 20.

Table 19: N_2 nominal pumping speed of commercial StarCell[®] SIP ('saturated') for different standard pump inlet diameters

| Pump inlet diameter DN [mm] | S_{N_2} [ℓs^{-1}] |
|--------------------------------|-----------------------------|
| 63 | 50 |
| 100 | 70 and 125 |
| 150 | 240 and 500 |

Table 20: Nominal pumping speed normalized to that of air for diode and triode SIP

| Gas | Air | N_2 | O_2 | H_2 | CO | CO_2 | H_2O | CH_4 | Ar | He |
|--------|-----|-------|-------|-------|-----|--------|--------|--------|------|-----|
| Diode | 1 | 1 | 1 | 1.5-2 | 0.9 | 0.9 | 0.8 | 0.6-1 | 0.03 | 0.1 |
| Triode | 1 | 1 | 1 | 1.5-2 | 0.9 | 0.9 | 0.8 | 0.6-1 | 0.25 | 0.3 |



Fig. 57: Cut view of a triode Star Cell pump. The inlet flange is DN63CF.

5.2.2 Getter pumps

Getter materials fix gas molecules on their surface by forming stable chemical compounds. The chemical reaction is possible only if the getter atoms are not already combined with surface contaminations, i.e. oxygen, carbon, etc. A contamination-free surface may be produced in two ways:

- sublimating the getter material in situ: evaporable getters or sublimation pumps;
- dissolving the surface contamination into the bulk of the getter material by heating: Non Evaporable Getters (NEG). The dissolution process is called activation.

A getter surface is characterised by its sticking probability α , namely the capture probability per molecular impingement. From Eq. 32, the pumping speed of getter material is written as:

$$S = \alpha A_{\text{getter}} C' \quad (84)$$

where A_{getter} is the geometric surface area of the getter material. α depends on many variables, first of all the nature of the gas. Getter materials do not pump rare gases and methane at room temperature. In that respect, they always need auxiliary pumping to keep a stable pressure. The sticking probabilities of homonuclear diatomic molecules are in general lower than that of molecules composed of dissimilar atoms. The values of α for common gas species in vacuum systems may be ordered in a growing series as follows:



For N_2 typical α are in the high 10^{-3} to low 10^{-2} range; for CO and CO_2 , α close to 1 may be measured. In addition, the sticking probability is strongly dependent on the gas surface coverage, i.e. the quantity of gas previously pumped on the getter material. As the gas surface coverage increases, the sticking probability decreases. The pumping becomes negligible when the surface is fully covered by gas molecules. As an example, complete saturation of a smooth NEG surface is obtained when about 10^{15} CO molecules cm^{-2} are adsorbed. Quantities about 5-10 times higher are reported for H_2O and O_2 . H_2 dissociates on the getter surface and diffuses into the bulk of the NEG material. As a result, its pumping does not block the adsorption of other molecules. The pumping capacity of hydrogen is orders of magnitude higher than that for other gas species.

The surface roughness has also a strong impact on the sticking probability. A single molecular arrival may result in several collisions with a rough getter surface, therefore enhancing the capture probability. The pumping capacity per geometric area is also increased.

Due to the high mobility of H atoms and the relatively low binding energy, the pumping of this gas is reversible: H_2 may be released by heating. The opposite effects of pumping and desorption

set up an equilibrium pressure P_{H_2} that depends on heating temperature T and hydrogen concentration c_H . The three variables are correlated by the Sievert's law (see Eq. 54). In Eq. 85 it is written in the logarithmic form.

$$\log P_{H_2} = A + 2 \log c_H - \frac{B}{T} \quad (85)$$

A and B are typical values for a given getter material.

5.2.2.1 Sublimation pumps

In particle accelerators, Ti is the only getter material used as evaporable getter. It is sublimated on the inner walls of a dedicated vessel from Ti-Mo filaments heated up to 1500°C. The maximum sticking probability varies in the range 1-5 10^{-2} for H_2 and 0.5-1 for CO. In some cases, the wall of the sublimation pumps may be cooled to liquid nitrogen temperature. In this case, the sublimated film is rougher and consequently the sticking probabilities are higher.

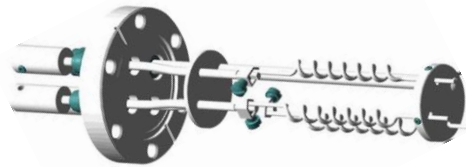


Fig. 58: Ti wires of a sublimation pump.
Courtesy of Kurt J. Lesker Company

When the deposited film is saturated, a new sublimation is needed to recover the initial pumping speed. A single filament withstands tens of sublimation cycles.

Sublimation pumps provide very high pumping speeds for a relatively low cost and have a limited maintenance. They are in general used to achieve pressures in the UHV range. Operation with continuous sublimation in higher-pressure ranges may be conceived; in this case cooling of the pump envelope must be added.

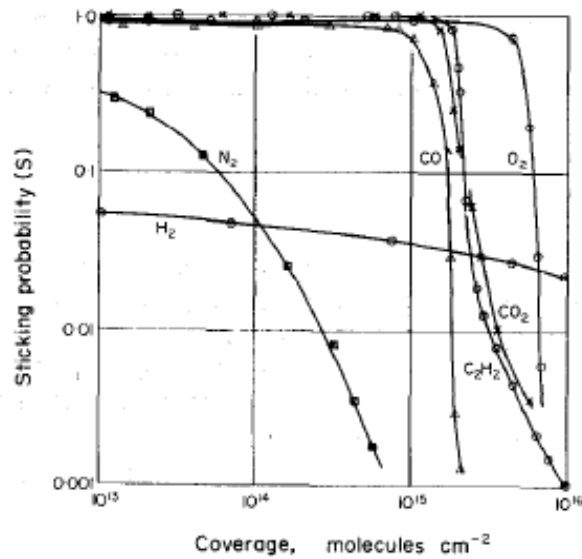


Fig. 59: Typical single-gas-coverage dependence of the pumping speed of sublimation pumps for selected gas species. This plot and other interesting measurements with sublimation pumps may be found in the very instructive paper of Ref. [35].

5.2.2.1 Non-evaporable getter pumps

During the activation process, the native oxide layer is dissolved in the NEG material. This relocation is possible only if it is energetically feasible and the bulk of the material has a large solubility limit for oxygen. Only few elements have these peculiar characteristics. Amongst them, those of the fourth group (Ti, Zr, and Hf) are the most relevant. These metals are able to dissolve oxygen at room temperature to more than 20% in atomic concentration. Other metallic elements are added to increase oxygen diffusivity and so reduce the activation temperature and time; this is typically the case of V. For specific purposes, other elements may be added in the alloy, for example to reduce pyrophoricity in air.

NEG materials are usually produced in powder form to increase the surface exposed and the pumping capacity. The powdered materials are either sintered to form disks and pellets or pressed on metallic substrates shaped as filaments and ribbons. The latter have found an extensive application in particle accelerator as linearly distributed pumps [36] (see Fig. 60). Thin-film NEG coatings produced by magnetron sputtering are also used in modern accelerators in the UHV pressure range [37].

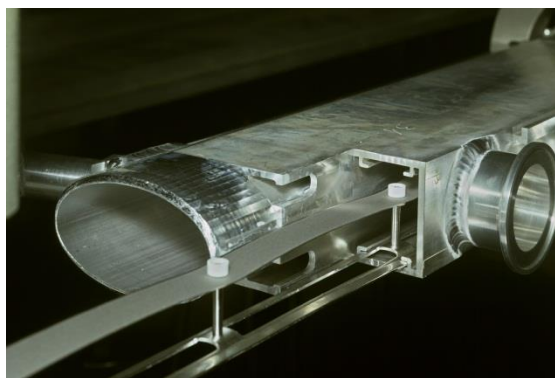


Fig. 60: Photograph of the dipole magnet vacuum chamber of the Large Electron Positron collider. The NEG pump is made of Zr-Al powder fixed on both side of a constantan ribbon.

A typical NEG alloy commercialised by SAES Getter (Milan, Italy) is the St707 made of Zr-V-Fe. It is activated at 400°C for 1 h or at 300°C for about 24 h; such characteristics allow passive activation during the bakeout of stainless steel vacuum chamber.

Modern lump NEG pumps provide gas surface capacities about 200 times higher than smooth surfaces. The embrittlement of the NEG elements limits the maximum quantity of H₂ that may be dissolved in the pumps. A safe limit of 20 Torr ℓ/g is given by SAES Getter for the St707. For the same alloy, the H₂ equilibrium pressure is shown in Fig. 61 for some temperatures.

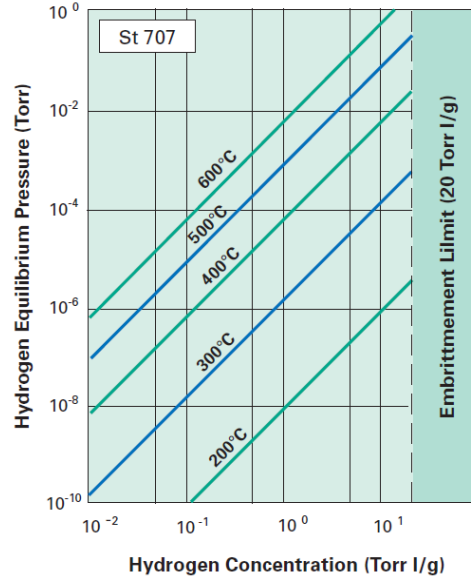


Fig. 61: Hydrogen equilibrium pressure for the St707 alloy. Courtesy of SAES Getters.

The constant A and B of Eq. 50 are 4.8 and 6116 when the pressure is expressed in Torr and the concentration in Torr ℓ g⁻¹.

After the pumping of a large quantity of H₂, a regeneration of the NEG pump may be necessary to avoid embrittlement. To do so, the NEG material is heated and the released gas is removed by a turbomolecular pump. The duration of the regeneration (t_R) is given by Eq. 86 [38]:

$$t_R = \frac{M_{NEG}}{S_{TMP}} \left(\frac{1}{q_f} - \frac{1}{q_i} \right) 10^{-\left(A - \frac{B}{T}\right)} \quad (86)$$

M_{NEG} (g) is the mass of the NEG material, S_{TMP} (ℓ s⁻¹) the pumping speed of the turbomolecular pump, q_i and q_f (Torr ℓ g⁻¹) the initial and the final concentration of hydrogen, T the temperature in K.

At room temperature, the pumping speed decreases as a function of the amount of gas pumped, except for H₂ that diffused into the alloy. The drop of pumping speed is less pronounced than for the sublimation pumps; this is due to high porosity and related surface area of commercial NEG materials (see Fig. 62). The SAES CapaciTorr pumps (see Fig. 63) have a sorption capacity for CO at room temperature up to about 5 Torr ℓ (~1.5 10²⁰ molecules). NEG pumps may operate at higher temperatures; the diffusion of C and O atoms is enhanced and the surface capacities largely increased.

The practical result is a less pronounced pumping speed drop as a function of the quantity of gas pumped. However, the H₂ release might be an obstacle to achieve the required pressure.

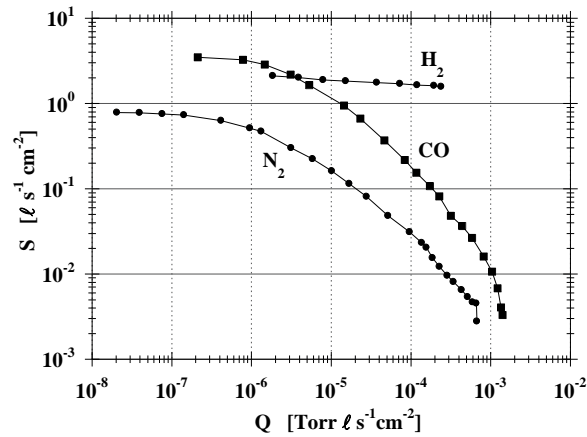


Fig. 62: Typical single-gas-coverage dependence of the pumping speed of a St 707 ribbon for selected gas species. This plot and other interesting measurements with NEG ribbons may be found in [39].

CO and CO₂ pumping hinder the adsorption of all other gases, while N₂ has only a limited effect and H₂ leaves the NEG surface unaffected.

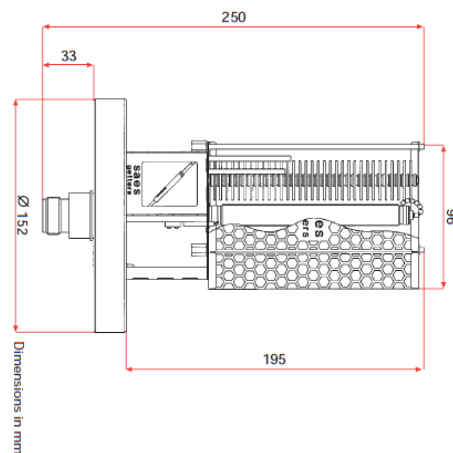


Fig. 63: Drawing and dimensions of a CapaciTorr pump. Courtesy of SAES Getters.

5.2.2.1 Non-evaporable getter thin film coatings

In progress...

5.2.3 Cryopumps

Cryopumps rely on three different pumping mechanisms:

- *Cryocondensation*: it is based on the mutual attraction of similar molecules at low temperature. The key property is the saturated vapour pressure P_v , i.e. the pressure of the gas phase in equilibrium with the condensate at a given temperature. The lowest pressure attainable by cryocondensation pumps is limited by the saturated vapour pressure. Amongst all gas species, only Ne, H₂ and He have P_v higher than 10^{-11} Torr at 20 K. The P_v of H₂ at the liquid He boiling

temperature is in the 10^{-7} Torr range, 10^{-12} Torr at 1.9 K. The quantity of gas that may be cryocondensated is very large and limited only by the thermal conductivity of the condensate.

- *Cryosorption*: it is based on the attraction between gas molecules and substrates. The interaction forces with the substrate are much stronger than those between similar molecules. As a result, providing the adsorbed quantity is lower than one monolayer, the sojourn time is much longer and gas molecules are pumped at pressure much lower than the saturated vapour pressure. Significant quantity of gas may be pumped below one monolayer if porous materials are used; for example, in one gram of standard charcoal for cryogenic application, about 1000 m^2 of surface are available for adsorption. The important consequence is that significant quantities of H_2 and He may be pumped at 20 K and 4.3K, respectively. In general, sub-monolayer quantities of all gas species are effectively cryosorbed at their own boiling temperature.

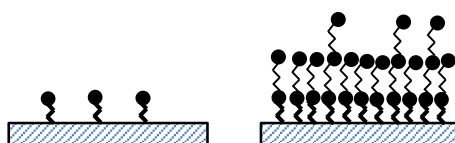


Fig. 64: Schematic drawing depicting sub-monolayer cryosorption (molecule-substrate interaction) and cryocondensation where the leading mechanism is inter-molecular interaction.

- *Cryotrapping*: the molecules of a low boiling temperature gas are trapped in the condensation layer of another gas. This is possible because the interaction energy between dissimilar molecules may be much higher than that between similar molecules. The trapped gas has a saturated vapour pressure several order of magnitude lower than in its pure condensate. Typical examples are Ar trapped in CO_2 at 77 K and H_2 in N_2 at 20 K.

Modern cryopumps exploit the first two mechanisms. The cryocondensation takes place on a cold surface, in general at 80 K for water vapour and at 10-20 K for the other gas species. The cryosorption of He, H_2 , and Ne is localised on a hidden surface coated with a porous material. This part of the pump is kept out of the reach of the other type of molecules, i.e. they have a probability close to one to be intercepted and adsorbed by other surface before reaching the cryosorber (see Fig. 65). The cooling is obtained by He gas cooled by Gifford-McMahon cryocooler.

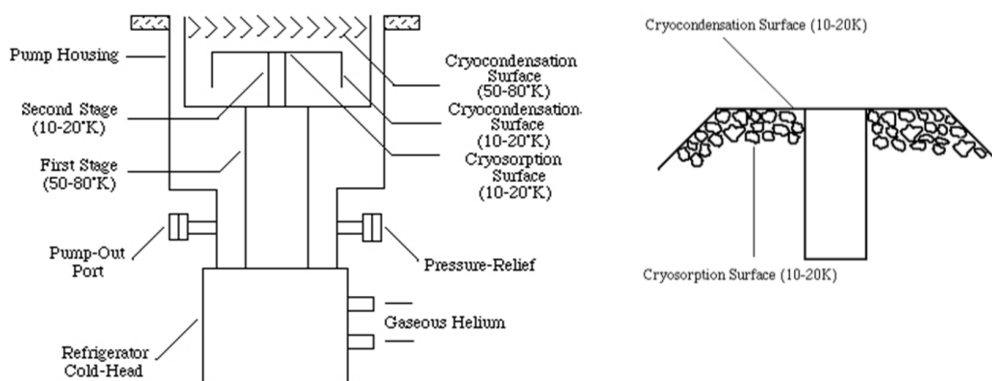


Fig. 65: Drawing of a generic cryopump with a closer view to the cryosorption surface where the porous material is fixed.

Cryopumps having pumping speeds in the range 800-60000 $\ell \text{ s}^{-1}$ are commercially available. For the condensable gas molecules, the capture probability is close to 1 (for example for water vapour). The maximum gas capacity (also called maximum gas intake) for the condensable gas is limited only by the thermal conductivity of the condensate. To avoid thick condensate layer and excessive thermal load, cryopumps should be started in molecular regime ($P < 10^{-3}$ mbar). The quantity and property of the porous material determine the maximum gas intake of cryosorbed gas. In general, it is orders of magnitude lower than that for the condensable gas.

Table 21: Pumping speeds and maximum gas capacities of a commercial cryopump (Oerlikon-Leybold 800 BL UHV); the pump inlet diameter is 160 mm.

Courtesy of Oerlikon-Leybold

| | H₂O | N₂ | Ar | H₂ | He |
|--|-----------------------|----------------------|-----------|----------------------|-----------|
| S [$\ell \text{ s}^{-1}$] | 2600 | 800 | 640 | 1000 | 300 |
| Capacity [Torr ℓ] | | 225000 | 225000 | 3225 | 375 |

Cryopumps require periodic regeneration to evacuate the gas adsorbed or condensed; in this way, the initial pumping speed is fully recovered. To do so, the cryopumps are warmed up to room temperature and the released gas is removed by mechanical pumps (mobile TMP in particle accelerators). During regeneration, the pump is separated from the rest of the system by a valve.

Excessive gas adsorption on the cryosorber leads to performance deterioration. A partial and much faster regeneration (1 h against more than 10 h) may be carried out at temperatures lower than 140°C in a way to remove the sorbed gas without releasing water vapour from the pump stage at higher temperature.

5.3 Comparison of pumps for ion sources

All pumps presented in the previous chapters have been used (or are going to be used) in the vacuum systems of ion sources and in their adjacent vacuum sectors. The choice is based not only on the gas load and required pressure, but also on the costs of the pumps, their maintenance, the duty time of the source, and safety aspects. Advantages and disadvantages of the four types of pumps presented in this note are summarised in Tab.22.

Table 22: Advantages and disadvantages of the presented types of pumps

| Type of pump | Advantages | Disadvantages |
|---------------------|--|---|
| TMP | <ul style="list-style-type: none"> - No memory effects - Constant pumping speed for pressures lower than 10^{-3} mbar - Pumping speed independent of total gas load - Starts working at high pressures (molecular regime) | <ul style="list-style-type: none"> - Mechanical fragility - Risk of contamination from the backing pump - Need of venting anytime the pump is stopped - Need of valve on the inlet flange - Intrinsic limitation in ultimate pressure of H₂ - Possible vibrations - Regular maintenance |
| SIP | <ul style="list-style-type: none"> - Clean pumping - No maintenance - No vibrations - Installation in any orientation | <ul style="list-style-type: none"> - Low capture probability - Gas selectivity and limited capacity - Memory effects (in particular for rare gases) - Ignition not recommended in the 10^{-3}-10^{-4} mbar |

| | | |
|--------------------|---|---|
| | <ul style="list-style-type: none"> - Relatively long lifetime - Relatively low cost - Limited but high H₂ capacity - The pump current gives a pressure reading | <ul style="list-style-type: none"> range - Heavy due to permanent magnets - Difficult starting for old pumps - Production of charged particles in particular at start-up - Field emission problems for old pumps - Fringing magnetic field - Safety issue: high voltage |
| Sublimation | <ul style="list-style-type: none"> - Clean vacuum - High pumping speed for reactive gases - With SIP, extremely low vacuum can be achieved - Low cost per ℓ/s - Electrical power only for sublimation; it works in case of power cut - Limited maintenance (filament change) - No vibration | <ul style="list-style-type: none"> - Very limited surface gas capacity - Need frequent sublimations at high pressure - Ti film peel-off for high sublimation rates - Selective pumping (no pumping of rare gases and methane) - Risk of leakage current in high voltage insulators |
| NEG | <ul style="list-style-type: none"> - Clean vacuum - High pumping speed for reactive gases - With SIP, extremely low vacuum can be achieved - High gas capacity for porous NEG - Low cost per ℓ/s - Electrical power needed only for activation; it works in case of power cut - No maintenance - No vibration | <ul style="list-style-type: none"> - Selective pumping (no pumping of rare gases and methane) - H₂ embrittlement if regeneration cannot be applied - Formation of dust particles is not excluded - Safety issue: pyrophoric, it burns when heated in air at high temperature |
| Cryo | <ul style="list-style-type: none"> - Very large pumping speed for all gases - Clean vacuum - High pumping capacity - Limited selectivity | <ul style="list-style-type: none"> - Cost and maintenance - Relatively large volume needed (including refrigerator) - Gas release in case of power cut - Reduced pumping efficiency for H₂ for high quantity of gas adsorbed: regeneration needed - Need of valve on the inlet flange |

6 Vacuum instrumentation

In progress...

8 The vacuum system of the Linac4 H- source

Linac4 is a linear accelerator, under construction at CERN, conceived in the framework of the high-intensity and high-luminosity upgrade of the LHC. It will be connected to the LHC injection chain at the latest during the LHC long shutdown 2 (LS2) [39].

In the first sections of Linac4, the main gas loads are the pulsed H_2 injection in the source and the continuous injection of the same gas in the Low Energy Beam Transfer (LEBT) for beam charge compensation. The vacuum system must evacuate the injected gas and ensure a pressure lower than $5 \cdot 10^{-7}$ mbar in the RFQ.

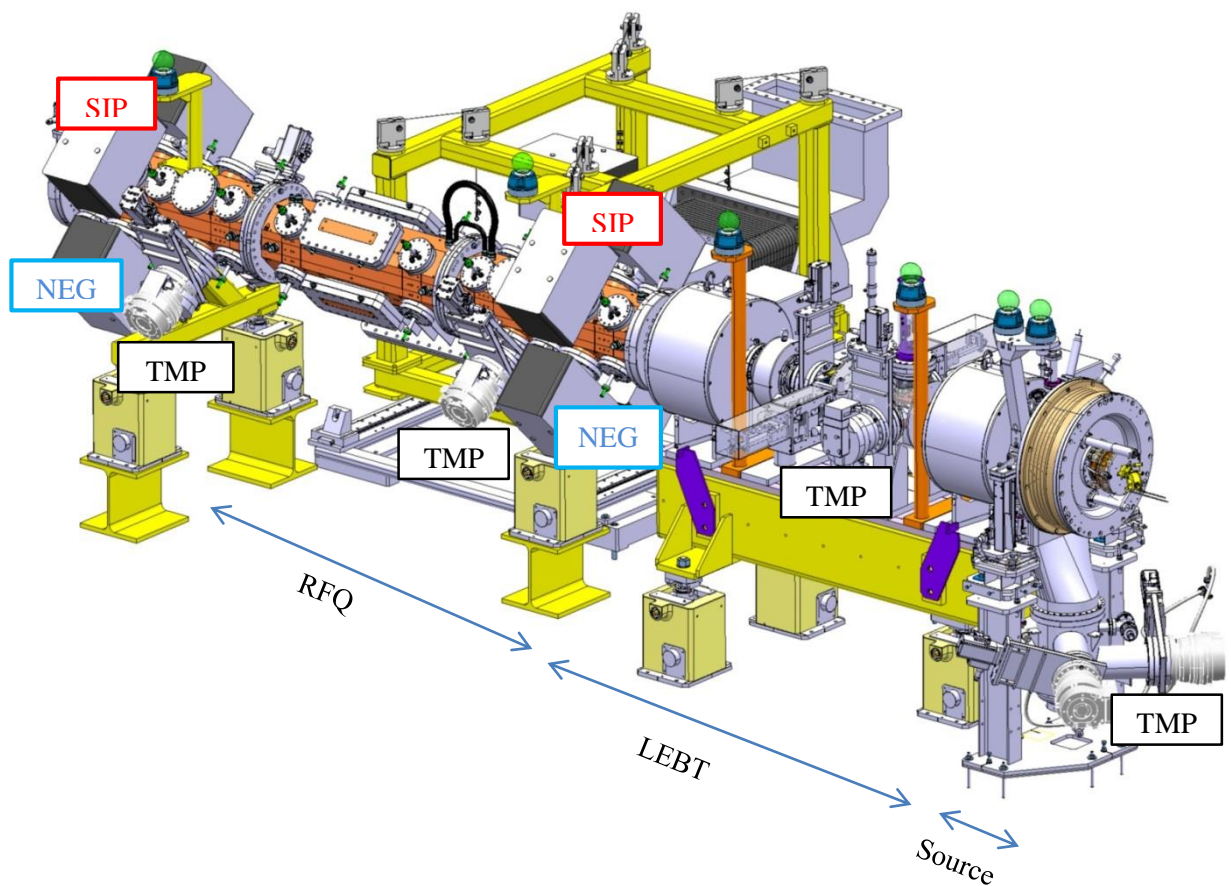


Fig. 66 Linac4 layout from the source to the RFQ. Courtesy of D. Steyaert, CERN EN-MME.

Fig. 66 shows the layout of the source up to the end of the RFQ. The extraction region of the source is equipped with two TMP that evacuate most of the pulsed flux from the source. An additional TMP is connected to the LEBT diagnostic tank to pump the local continuous injection of H_2 . The RFQ is divided into three tanks. SIP, NEG pumps and TMP are installed on the first and the third tank. The NEG pumps provide high pumping speed and capacity for hydrogen. The SIPs contribute to the H_2 pumping and ensure the removal of gas species that are not pumped by getters. The TMP are backup pumps in case a problem occurs.

The electrical-network vacuum analogy was applied to evaluate the time dependent pressure profiles from the source to the end of the RFQ. Fig. 67 and 68 shows the H_2 partial pressures profiles as a function of time and position. Two situations are illustrated, i.e. the pressure profiles with and without continuous injection in the LEBT. A detailed analysis of the vacuum system of the Linac4 source can be found in [16].

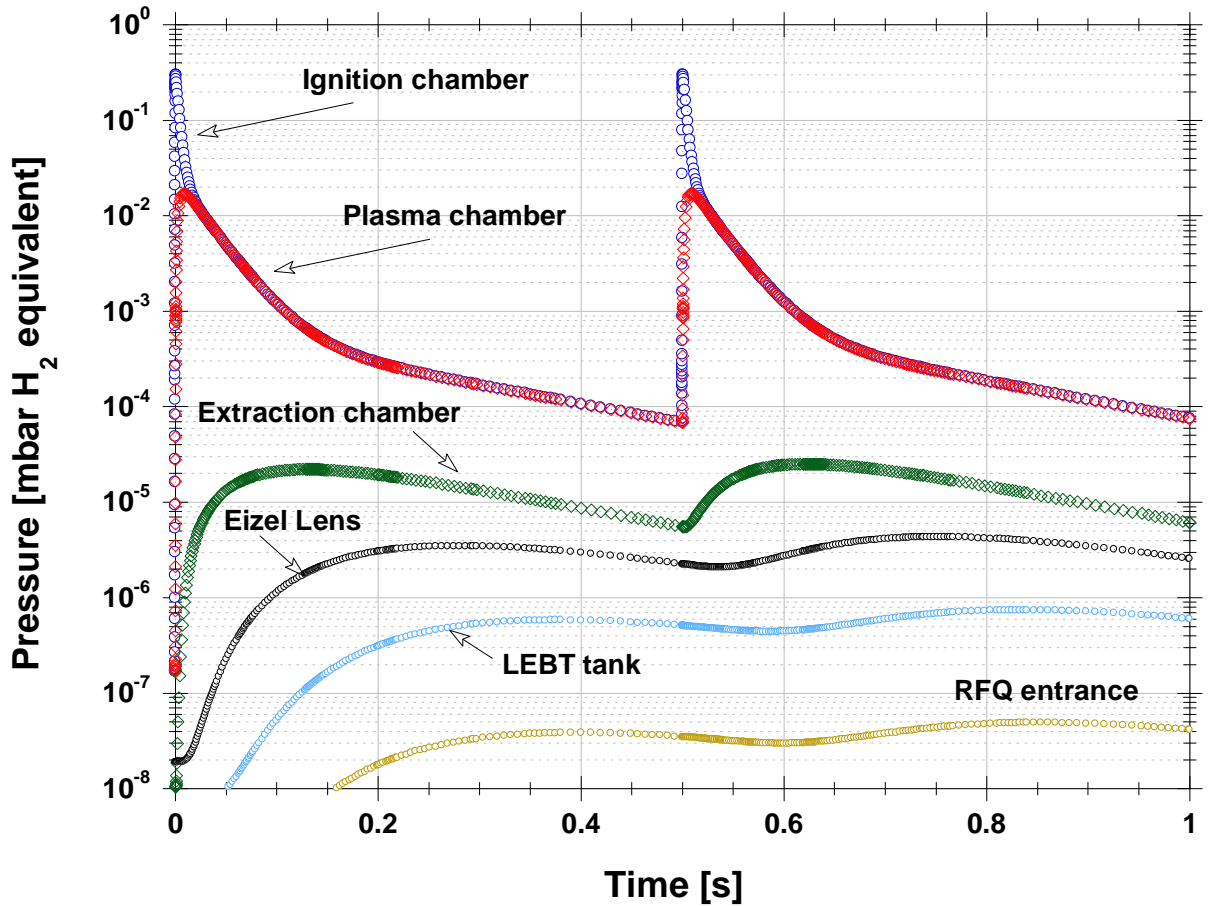


Fig. 67: Calculated H_2 pressure variations in the Linac4 H^+ source. The H_2 gas burst from the piezovalve is about $5 \cdot 10^{-3}$ mbar ℓ per pulse; each pulse lasts $5 \cdot 10^{-4}$ s at a repetition frequency of 2 Hz. In this example, the injection in the LEBT is not taken into account.

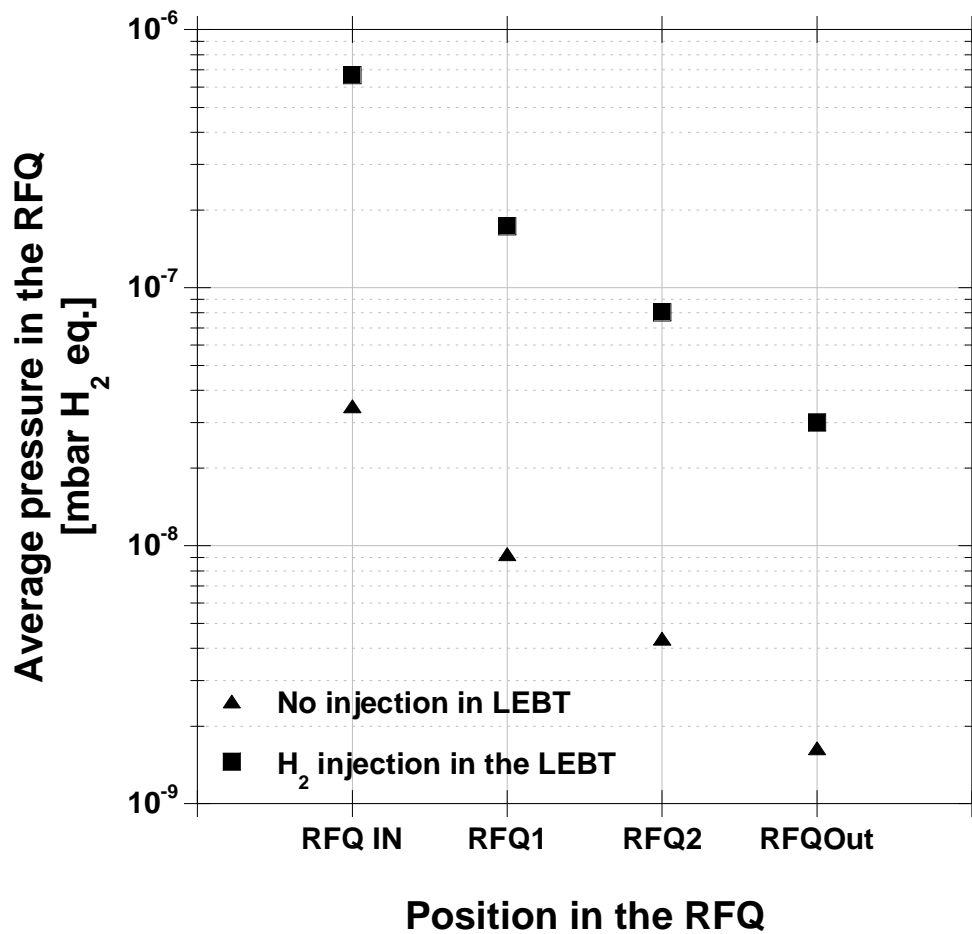


Fig.68: Pressure profiles in the RFQ of Linac4 with and without H₂ injection in the LEBT. For the calculation, the injection in the LEBT is equivalent to fixing the pressure in the LEBT to 10⁻⁵ mbar (H₂ equivalent).

Acknowledgement

I wish to thank all my colleagues of the Vacuum, Surfaces and Coatings group of the Technology Department at CERN, including students and visitors. The VSC group has become a centre of excellence in Europe for vacuum technology encompassing all aspects, from surface treatments to computation, operation, and control of unique facilities. A significant part of my experience originates from years of work I have been sharing with them.

References

- [1] C. Benvenuti and M. Hauer, Proceedings of Eight International Vacuum Congress Cannes, 1980, vol II, 199–202; available in CERN Document Server at <http://cdsweb.cern.ch/record/314288/files/CM-P00064854.pdf>
- [2] Sir James Jeans, *An Introduction to the Kinetic Theory of Gases* (Cambridge University Press, Cambridge, 1967)
- [3] John B. Hudson, *Surface Science an Introduction* (John Wiley & Sons, 1998) p. 125.
- [4] Hans Kuhn, Horst-Dieter Försterling, David H. Waldeck, *Principles of Physical Chemistry, 2nd Edition* (John Wiley & Sons, 2009) p. 405.
- [5] Karl Jousten (Ed.), *Handbook of Vacuum Technology Book* (Verlag-VCH, Weinheim, 2008)
- [6] James M. Lafferty (Ed.), *Foundations of Vacuum Science and Technology* (John Wiley and Sons, 1998)
- [7] P. Clausing, Ann. Phys. 12 (1932) 961; republished in J. Vac. Sci. Technol. 8 (1971) 636
- [8] A. Berman, *Vacuum Engineering calculation, Formulas, and Solved Exercises* (Academic Press, 1992)
- [9] Donald J. Santeler, J. Vac. Sci. Technol A, 4 (1986) 348
- [10] J. Cole, Prog. Astronaut. Aeronaut. 51 (1976) 261 and D.H Davis, J. Appl. Phys. 31 (1960) 1169
- [11] R. Kersevan and J.-L. Pons J. Vac. Sci. Technol. A **27** (2009) 1017; Molflow+ are available at <http://test-molflow.web.cern.ch/>
- [12] P. Chiggiato, CERN-ATS-Note-2012-048 TECH (in French); lecture given at CAS on Vacuum in Particle Accelerators 2006: <http://cas.web.cern.ch/cas/Spain-2006/Spain-lectures.htm>
- [13] R. N. Peacock, J. Vac. Sci. Technol., 17 (1980) 330
- [14] A. Rossi, LHC Project Note 341, 2004; available at the CERN library: <http://cdsweb.cern.ch/record/728512/files/project-note-341.pdf?version=1>
- [15] Christina Yin Vallgren et al., CERN ATS-Note-2012-041 TECH; available at the CERN library: http://cdsweb.cern.ch/record/1445914/files/ATSnote_final.pdf
- [16] Chiara Pasquino et al., CERN-ATS-Note-2012-043 TECH; available at the CERN library: http://cdsweb.cern.ch/record/1447099/files/ATS_Note%20-LINAC4%20H-%20source.pdf
- [17] H.F. Dylla, D. M. Manos, P.H. LaMarche Jr. J. Vac. Sci. Technol. A11 (1993) 2623
- [18] K. Kanazawa, J. Vac. Sci. Technol. A7 (1989)
- [19] R. N. Peacock, J. Vac. Sci. Technol., 17 (1980) 330\$
- [20] M. C. Bellachioma, PhD Thesis, Università di Perugia, CERN-THESIS-2004-060.
- [21] W.Prins and J.J.Hermans, J.Phys.Chem. 63 (1959) 716.
- [22] J. Gomez-Goni and A. G. Mathewson, J. Vac. Sci. Technol. A15 (1997) 3093
- [23] P. A. Redhead, J. P. Hobson, E. V. Kornelsen, *The Physical Basis of Ultrahigh Vacuum*, (Chapman and Hall, 1968), p. 167
- [24] T. E. Madey, D. E. Ramaker and R. Stockbauer, Ann. Rev. Phys. Chem. 35 (1984) 215-240
- [25] R. D. Ramsier and J. T. Yates Jr, Surface Science Report 12 (1991) 243-378
- [26] Foester, Halama, Lanni, J. Vac. Sci. Technol. A8 (1990) 2858
- [27] J. Gomez-Goni et al. J. Vac. Sci. Technol. A12 (1994) 1714

- [28] J. Schou, CAS, Vacuum in Accelerators
- [29] G. Hulla, CERN-THESIS-2009-026
- [30] E. Mahner, Phys. Rev. ST Accel. Beams 11 (2008) 104801.
- [31] O. Gröbner, R. Calder, PAC73, San Francisco USA, March 5-7, p. 760, 1973
- [32] I. R. Collins et al., LHC Project Report 312, 1999
- [33] J. Frenkel, Z. Physik, 26 (1924) 117
- [34] Kimo M. Welch, *Capture Pumping Technology*, (North-Holland Elsevier, 2001), p. 106
- [35] A. K. Gupta and J. H. Leck, Vacuum, 25 (1975) 362
- [36] C. Benvenuti, Nuclear Instruments and Methods 205 (1983) 391
- [37] C. Benvenuti, Proc. of EPAC 1998, Stockholm;
<http://accelconf.web.cern.ch/AccelConf/e98/PAPERS/THZ02A.PDF>
- [38] B. Ferrario, Proc. 9th Symp. on Fusion Technology, Garmisch Partenkirchen, 1976
- [39] C. Benvenuti and P. Chiggiato, J. Vac. Sci. Technol., A14 (1996) 3278
- [40] L. Arnaudon et al. CERN-ATS-2011-041; available at the CERN library:
<http://cdsweb.cern.ch/record/1378473/files/CERN-ATS-2011-041.pdf>